International Journal of Nanomedicine

Dovepress
open access to scientific and medical research

Open Access Full Text Article

ORIGINAL RESEARCH

Multifunctional Theranostic Nanoparticles for Enhanced Tumor Targeted Imaging and Synergistic FUS/Chemotherapy on Murine 4T1 Breast Cancer Cell

Zhengyue Kang[1,2,*], Min Yang[1,2,*], Xiaoling Feng[1,2], Hongjian Liao[1,2], Zhifei Zhang[1,2], Yonghong Du[1,2]

[1]State Key Laboratory of Ultrasound in Medicine and Engineering, College of Biomedical Engineering, Chongqing Medical University, Chongqing, 400016, People's Republic of China; [2]Chongqing Key Laboratory of Biomedical Engineering, Chongqing Medical University, Chongqing, 400016, People's Republic of China

*These authors contributed equally to this work

Correspondence: Yonghong Du, State Key Laboratory of Ultrasound in Medicine and Engineering, College of Biomedical Engineering, Chongqing Medical University, Chongqing, 400016, People's Republic of China, Tel/Fax +86-23-68485021, Email duyonghong@cqmu.edu.cn

Purpose: Triple negative breast cancer (TNBC) is challenging for effective remission due to its very aggressive, extremely metastatic and resistant to conventional chemotherapy. Herein, a multifunctional theranostic nanoparticle was fabricated to enhance tumor targeted imaging and promote focused ultrasound (FUS) ablation and chemotherapy and sonodynamic therapy (SDT). A multi-modal synergistic therapy can improve the therapeutic efficacy and prognosis of TNBC.

Methods: AS1411 aptamer modified PEG@PLGA nanoparticles encapsulated with perfluorohexane (PFH) and anti-cancer drug doxorubicin (DOX) were constructed (AS1411-DOX/PFH-PEG@PLGA) to enhance tumor targeted imaging to guide ablation and synergistic effect of FUS/chemotherapy. FUS was utilized to trigger the co-release of doxorubicin and simultaneously PFH phase transition and activate DOX for SDT effect. The physicochemical, phase-changeable imaging capability, biosafety of nanoparticles and multi-mode synergistic effects on growth of TNBC were thoroughly evaluated in vivo and in vitro.

Results: The synthesized AS1411-DOX/PFH-PEG@PLGA (A-DPPs) nanoparticles are uniformly round with an average diameter of 306.03 ± 5.35 nm and the zeta potential of −4.05 ± 0.13 mV, displaying high biosafety and FUS-responsive drug release in vitro and in vivo. AS1411 modified NPs specifically bind to 4T1 cells and elevate the ultrasound contrast agent (UCA) image contrast intensity via PFH phase-transition after FUS exposure. Moreover, the combined treatment of A-DPPs nanoparticles with FUS exhibited significantly higher apoptosis rate, stronger inhibitory effect on 4T1 cell invasion in vitro, induced more reactive oxygen species (ROS), and enhanced anti-tumor effect compared to a single therapy ($p < 0.05$). Additionally, the joint strategy resulted in more intense cavitation effect and larger ablated areas and reduced energy efficiency factor (EEF) both in vitro and in vivo.

Conclusion: The multifunctional AS1411-DOX/PFH-PEG@PLGA nanoparticles can perform as a marvelous synergistic agent for enhanced FUS/chemotherapy, promote real-time contrast enhanced US imaging and improve the therapeutic efficacy and prognosis of TNBC.

Keywords: focused ultrasound, multifunctional nanoparticle, synergistic therapy, phase transformation, acoustic cavitation, breast cancer

Introduction

Breast cancer is one of the most malignant cancers in women worldwide, which caused the second most death cases of tumors in women worldwide in 2020.[1] Triple negative breast cancer (TNBC) is a subgroup of breast cancer that lacks expressions of the estrogen receptor (ER), progesterone receptor (PR), and human epidermal growth factor receptor 2 (HER2).[2,3] Regrettably, TNBC is challenging for oncologists due to its very aggressive, extremely metastatic and resistant to conventional chemotherapy, which is difficult to be treated for effective remission by

Received: 11 February 2022
Accepted: 1 May 2022
Published: 13 May 2022

relying only on conventional chemotherapeutic drugs or other physical therapy. Recently, combination therapy has become an important strategy for minimizing side effects and enhancing the therapeutic outcomes of cancer treatment.[4]

Focused ultrasound (FUS), as a non-invasive treatment that has been widely used in the treatment of solid tumors, is a new choice to improve the therapeutic efficacy and overcome the drug resistance to the TNBC treatment.[5,6] However, for some advanced TNBC patients whose tumors were always in diabrosis and their physical condition was poor, which prevented them from receiving the hyperthermia ablation during higher energy FUS treatment with a series of severe side effects, such as skin burns, nerve damage and transient pain would appear.[7] In order to improve the ablation efficiency of high-intensity FUS at lower energy, the introduction of effective synergistic agents in the FUS ablation process is expected to solve the problems of incomplete treatment and recurrence.

Nanoparticles (NPs) with smaller size, longer blood-circulation time, good stability and easy surface modification may be the effective synergistic agents via increasing the cavitation effect to kill tumor cells in the FUS ablation process.[8,9] However, the diameters of nanoscaled agents limit their capability to generate back-scattering echo signals for real-time contrast enhanced ultrasound (CEUS) imaging. In recent years, liquid fluorocarbon perfluorohexane (PFH) with a low boiling point (56°C) and liquid-gas phase transition characteristics are generally enclosed in liposomes, polymer, or albumin shells to facilitate tumor imaging. Importantly, studies have demonstrated that NPs containing PFH can be triggered by thermal effect of FUS to undergo the liquid-gas phase transition, which could be used to assist the contrast-enhanced US (CEUS) imaging and therapeutic monitoring of the tumor.[10,11]

Doxorubicin (DOX) is famous as not only one of the most universally used chemotherapeutic drugs for treating various tumors but also one of the well-known effective sonosensitizers with sonodynamic therapy (SDT) effect after interaction with ultrasound.[12,13] However, owing to the insufficient quantity of drugs available in the breast tissue even when systemically administered at very high doses and serious dose-dependent DOX-induced cardiotoxicity, its clinical application in TNBC therapy has been progressively limited.[14] To circumvent most of these hurdles, various nano drug delivery systems have been constructed to greatly reduce drug toxicity and exerted the specific functionality as either ultrasound-based contrast agents or ultrasound-based synergistic agents for tumor diagnostic imaging and therapies.[15–17] Among various nano/micro-materials, Poly(ethylene glycol) (PEG)-functionalized PLGA NPs are especially desirable because PEGylation provided a hydrophilic layer on the surface of NPs to significantly prevent the rapid clearance of NPs by the reticuloendothelial system elimination, which is especially important for the passive targeting of nano-carriers to tumor by the enhanced permeability and retention (EPR) effects.[18]

Furthermore, except for the passive targeting of EPR effect, a specific active selection and efficient drug delivery design is the key to achieving precision imaging and treatment of solid tumors. Compared to conventional targeting agents such as antibodies, peptides, small molecules, DNA aptamers have attracted remarkable attention in the design of active drug delivery systems benefit from the advantages of low molecular weights, lack of immunogenicity, good stability and high specificity and affinity with target molecules.[19] AS1411, a 26-mer DNA aptamer with the G-quadruplex structure, has a strong binding affinity to nucleolin which is a protein highly expressed in the plasma membrane of cancer cells and has been successfully exploited as a targeting ligand for tracking 4T1 breast cells.[20,21]

Herein, we have successfully fabricated multifunctional theranostic nanoparticles for enhanced tumor targeted imaging and synergistic FUS ablation and chemotherapy on TNBC. Such a nano-theranostic agent is based on PLGA-PEG biomaterial as outer shell of NPs, FUS-responsive PFH and anticancer drug DOX as the core and the aptamer AS1411 was covalently linked onto the outer shell of NPs for targeting transportation and accumulation in tumor tissue (designated as AS1411-PFH/DOX-PEG@PLGA NPs). FUS was utilized to trigger the co-release of DOX and PFH, simultaneously PFH undergo a liquid-gas phase transition upon activation by the thermal effect of FUS to enhance tumor imaging and DOX be activated for sonodynamic therapy. The designed multifunctional theranostic AS1411-PFH/DOX-PEG@PLGA NPs mediated FUS/chemo therapy totally eradicated tumors with great biosafety in vitro and in vivo, providing a promising way to treat TNBC. Schematic illustrations of the designed multi-functional AS1411-PFH/DOX-PEG@PLGA nanoparticles and the procedure of the FUS/chemo therapy are shown in Scheme 1.

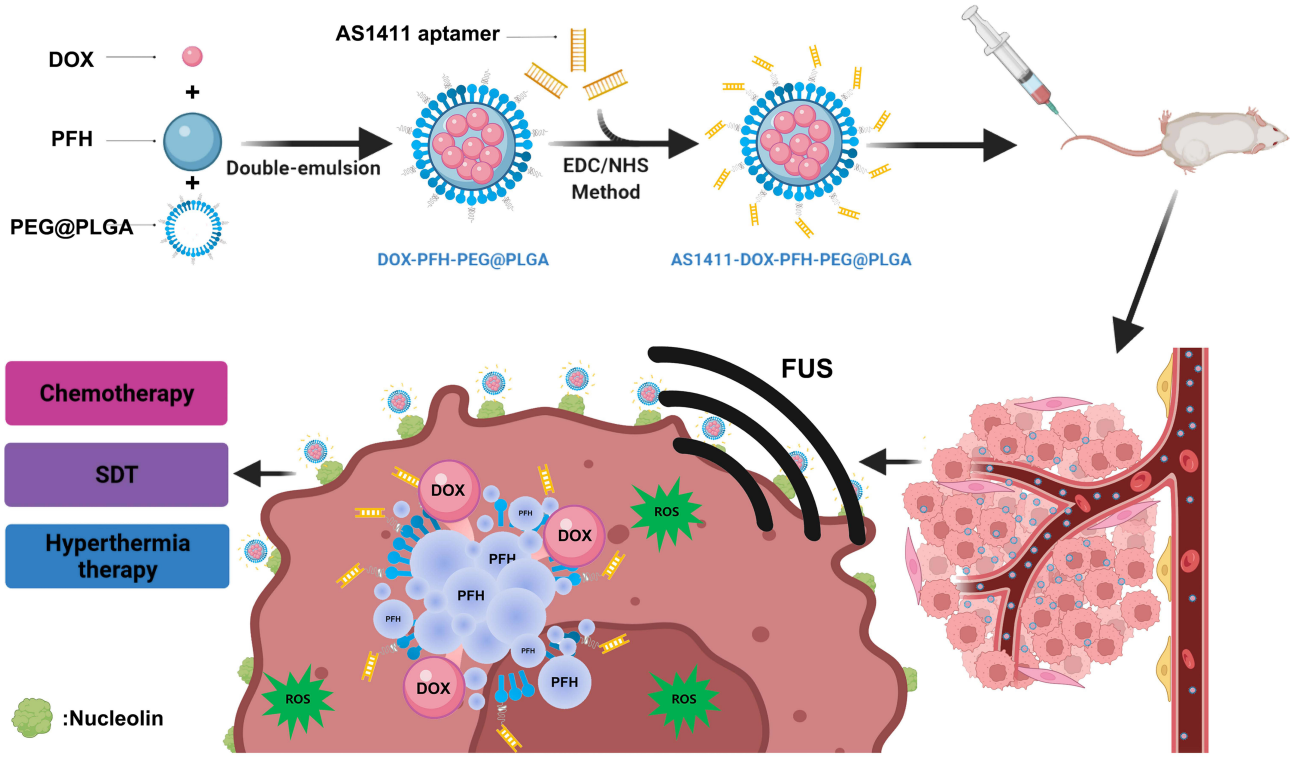

Scheme 1 Schematic demonstration of FUS/chemo synergistic therapy strategy.

Materials and Methods

Materials

PLGA-PEG50/50-COOH (MW 15000, Jinan Daigang Biotechnology Co., LTD.); Chloroform ($CHCl_3$, MW 119.38), isopropyl alcohol (MW 60.10, Chongqing Chuandong Co., LTD.); Polyvinyl alcohol (PVA, MW 30000–70000), Perfluorohexane (PFH, MW 338.04), 1,1-dioctadecyl-3,3,3′,3′-tetramethylindocarbocyanine perchlorate(DiI), 4’,6-diamidino-2-phenylindole (DAPI), 1-ethyl-3-(3-dimethylaminopropyl) carbodiimide (EDC, MW 191.70), N-hydroxysuccinimide (NHS, MW 115.09) were all purchase from Sigma Ltd. Co., (USA); 1,1′-dioctadecyl-3,3,3′,3′-tetramethylindotricarbocyanineiodide (DiR), 2,7-dichlorodihydrofluorescein diacetate (DCFH-DA) were bought from Beyotime Biotechnology Co., Ltd. (Shanghai, China). MES buffer (Thermo Fisher Scientific, USA); Doxorubicin (DOX, MW 579.98) (Aladdin, Shanghai, China); CCK-8 (Dojindo, Japan); 2′,7′-dichlorofluorescein diacetate (DCFH-DA) probe; Aptamer AS1411 and Aptamer FAM modified AS1411-NH_2 were purchased by ShengGong BIO Engineer Ltd. Co. (Shanghai, China) with a nucleotide sequence: (5′-GGTGGTGGT GGTTGTGGTGGTGGTGG-3′). The Focused Ultrasound Tumor Therapeutic System (Model-JC200, Chongqing Haifu Medical Technology Co., Ltd, Chongqing, China) was chosen to be the high-intensity FUS transducer.

Synthesis and Characterization of AS1411-DOX/PFH-PEG@PLGA Nanoparticles

PEG@PLGA nanoparticles integrated with PFH and DOX were prepared by the double-emulsion method. Briefly, 200 μL PFH and 5 mg DOX were added into 2 mL of $CHCl_3$ after dissolving 40 mg of PEG@PLGA crystals. The mixture was emulsified in an ice bath by using an ultrasonic probe (XL2020 Acoustic Vibrograph, USA) with the power of 150 W (70% amplitude) for 90s. Then, the emulsion was added into 4 mL of PVA solution (4% w/v) and sonicated for another 150s. The final solution was added to an 8 mL of isopropanol and placed in an ice bath overnight to stabilize the NPs and extract $CHCl_3$. Subsequently, the NPs were centrifuged at 1000 rpm for 10 min to remove impurities and washed with deionized water for three times repeatedly. The prepared DOX/PFH-PEG@PLGA nanoparticles (DPPs) were stored at temperature 4°C.

AS1411 aptamers were linked to the shell of PEG@PLGA nanoparticles via a carbodiimide reaction. First, the DPPs were resuspended in a MES buffer (0.1 M, pH = 5.5), where then agents EDC (molar ratio of PLGA and EDC was 1:10) and NHS

(mass ratio of EDC and NHS was 1:3) were added in an ice bath for 15 min with gentle stirring to activate PEG@PLGA NPs. The unreacted EDC and NHS were removed by centrifugation and the NPs were repeatedly cleaned. Then, the activated NPs and dissolved AS1411 aptamer were incubated with MES (0.1 M, pH = 8.0) buffer at room temperature overnight. The constructed AS1411-DOX/PFH-PEG@PLGA NPs (A-DPPs) were washed with MES buffer for three times to remove unbound aptamers. DiI or DiR fluorescence labeled nanoparticles, blank NPs and Dil-labeled A-DPPs with FAM fluorescent (FAM was modified at the 3′ end of AS1411-NH_2) were fabricated by the same procedures. AS1411-DOX-PEG@PLGA NPs (A-DPs) were constructed by the same procedure except that PFH was not added.

The mean size and zeta potential of nanoparticles were measured by utilizing Dynamic Light Scattering (DLS, Malvern Instruments, UK). Morphology and structure characterizations of the A-DPPs were observed by Transmission Electron Microscopy (TEM, Hitachi H-7600, Japan). During the continuous observation of changes of the scattered A-DPPs in fetal bovine serum (FBS) at 37°C, which focused on the mean size of A-DPPs within 1 week, and size were examined at Day 0, 1, 3, 7.

The linkage between AS1411 aptamer and DPPs was measured quantitatively and qualitatively. 10μL of 4.0 mg/mL DiI-labeled A-DPPs with FAM were taken onto the glass slide, and confocal laser scanning microscopy (CLSM, Nikon A1, Japan) was utilized to observe the successful conjugation between nanoparticles and AS1411 through the fluorescent fusion state. The connection rate was examined by the Flow Cytometry (Beckman Coulter, Inc., USA).

To determine the loading efficiency and encapsulation efficiency of drug DOX in A-DPPs, first the drug DOX standard curve was calculated through the absorbance intensities among varying concentrations of DOX (1, 5, 10, 20, 40, 50, 60, 70, 100, 125 μg/mL) by UV-vis spectrophotometer (UV-2600 SHIMADZU, Japan) at 480 nm. Then, loading content and encapsulation efficiency were counted as follows:

$$\text{LC } \% = (\text{weight of DOX in NPs/total weight of NPs}) \times 100\%$$

$$\text{EE } \% = (\text{weight of DOX in NPs/total weight of DOX}) \times 100\%$$

Cell Culture and Animal Models Establishment

The murine 4T1 breast cancer cell line and human normal liver cells (L-O2) were both obtained from Laboratory of Cytopathology, the First Affiliated Hospital of Chongqing Medical University. The L-O2 cells were authenticated by STR profile for accuracy of the study. 4T1 Cells were cultured in RPMI-1640 medium with 10% fetal bovine serum and 1% penicillin/streptomycin while L-O2 cells were cultured in DEME medium with 10% fetal bovine serum and 1% penicillin/streptomycin and all cells were preserved in a humidifier incubator containing 5% CO_2 at 37°C. All the cells used in the experiments were in logarithmic growth phase.

Female Balb/c mice (6–8 weeks old; weight of 16–21 g) were purchased from and raised at the Animal Experiment Center of Chongqing Medical University (Chongqing, China). To inoculate solid murine TNBC, the murine breast cancer cell line 4T1 cells were detached with trypsin and resuspended in sterile saline (pH = 7.4). Then, the logarithmic growth phase cells (1×10^6 cells/200 μL) were subcutaneously injected into the right flank of every mouse. All tumor-bearing mice were experimented when the volumes reached 100–150 mm^3 approximately. The use of the cell lines and experimental procedures involving human species and animals were approved by the ethics committee of Chongqing Medical University. All procedures involving animals were conducted with the guidelines of the Institutional Animal Care and Use Committee (IACUC) of Chongqing Medical University.

Cytotoxicity and Biosafety of A-DPPs

L-O2 human normal liver cell and 4T1 cells were planted in 96-well culture plates (1×10^4 cells/well) and incubated in the cell incubator (37°C, 5% CO_2) for 24 h. Sterilized A-DPPs were configured with serum-free cell culture medium at varying equivalent DOX concentrations (1.25, 2.5, 5.0, 10.0, 20.0, 40.0 μg/mL) and added into the 96-well culture plates. Subsequently, all the cells were cultured for 24 h and then washed with saline. Then, 10% CCK-8 reagent was added into every well at a dose of 100 μL for another 2 hours and the absorbance values of these cells at 450 nm wavelength were detected by the Multifunctional Enzyme Label Instrument (ELI, Thermo Fisher Scientific, USA). The wells containing

only medium without cells were set as the blank group and the wells with both cells and serum-free medium were regarded as the control group. Cell survival rate was calculated according to the formula as follows

$$\text{Cell Viability } (\%) = (\text{OD}_{\text{NPs}} - \text{OD}_{\text{blank}})/(\text{OD}_{\text{control}} - \text{OD}_{\text{blank}}) \times 100\%$$

Hemolysis assay was carried out as a standard biosafety test. First, blood samples were collected from healthy Balb/c mice. Red blood cells (RBCs) were isolated by centrifugation. The plasma was removed and the precipitated RBCs were retained and diluted with normal saline. Then, 100 μL blood samples were evenly mixed with A-DPPs of different concentrations (0.1, 0.25, 0.5, 1.0, 2.0, 4.0 mg/mL) and co-incubated at 37°C for 4 h. Finally, the samples were centrifuged at 1200 rpm for 3 min, and the supernatant was taken to a 96-well plate (100 μL/well). The absorbance value at 541 nm was read by multi-functional Enzyme Label Instrument (ELI, Thermo Fisher Scientific, USA). The hemolysis rate was calculated according to the following equation:

$$\text{Hemolysis rate } (\%) = \left(\text{OD}_{\text{sample}} - \text{OD}_{\text{negative}}\right)/\left(\text{OD}_{\text{positive}} - \text{OD}_{\text{negative}}\right) \times 100\%$$

$\text{OD}_{\text{sample}}$ is the value at each concentration level, $\text{OD}_{\text{negative}}$ is the value detected in the negative control (RBCs with deionized water), $\text{OD}_{\text{positive}}$ is the value tested in the positive control (RBCs with normal saline).

To confirm the biosafety of A-DPPs in vivo further, healthy female Balb/c mice were injected with 200 μL A-DPPs at a concentration of 4.0 mg/mL respectively via tail vein. Blood samples were collected for blood routine analysis and biochemistry analysis at 0d, 3d, 7 d and 14 d after injection, respectively. At the 14th day, the main organs (liver, spleen, kidney, heart and lung) of the mice were isolated, sliced and H&E stained for the evaluation of biocompatibility.

Releasing Behavior and Pharmacokinetics of Nanoparticles

The in vitro drug release pattern from nanoparticles was conducted via the dialysis method.[22] On account of the acid microenvironment of tumors, A-DPPs in different pH conditions without FUS stimulation were initially assessed. The same volume of nanoparticle solutions in 3 mL saline at two different pH (5.5 and 7.4) was placed in two dialysis bags (8–12 kDa MWCO, Spectrum Laboratories, CA, USA) and shaken at 120 rpm at 37°C. Then we further analyzed the DOX-releasing behavior of nanoparticles triggered by FUS. After 4 h releasing, the samples in pH 5.5 and pH 7.4 were exposed to FUS (1.0 MHz, 80 W/cm^2, 5 s), respectively, followed by shaking. At pre-determined time points (0, 1, 2, 4, 8, 12, 24, 48, 72 h), the DOX concentration of each sample was detected by using the UV-vis spectrophotometer.

We investigated the plasma pharmacokinetics of DOX released from A-DPPs in vivo through Balb/c mice bearing 4T1 tumors. Based on the DOX loading efficiency, Mice were injected intravenously with free DOX (1.5 mg/kg) and DPPs (DOX concentration 1.5 mg/kg) and A-DPPs (DOX concentration 1.5 mg/kg), respectively. At various time intervals (10 min, 30 min, 1, 2, 4, 8, 24 h) post i.v., blood sample was collected, centrifuged for 10 min (3000 rpm, 4°C) for 10 min, and 100 μL of the supernatant plasma was extracted using 900 μL of acetonitrile to precipitate all of the proteins. The organic phase was detected using UV−Vis spectrophotometry to measure the DOX concentration.

Targeting Ability Assay in vitro

The cell-targeting ability in vitro was confirmed qualitatively by CLSM. The cells were inoculated in the CLSM-exclusive culture dishes (1×10^5 /well) and incubated for 24 h. Then, all cells were divided into three groups: the Non-targeting group (4T1 and DiI-labeled DPPs), the Targeting group (4T1 and DiI-labeled A-DPPs) and the Negative control group (L-O2 cells and DiI-labeled A-DPPs). After the corresponding culture media were added, the three groups were placed into incubation for 4 h. Importantly, cells were fixed with 4% paraformaldehyde (15 min), stained by DAPI (10 min). During the mentioned process above, the cells were washed 3 times with saline per step to remove the untargeted NPs and residual dye. Eventually, the uptake of A-DPPs by cells was observed under the CLSM (Nikon, Japan). Meanwhile, the corresponding quantitative investigation of cell-targeting ability was performed by the Flow Cytometry (Beckman Coulter, Inc., USA).

Biodistribution and Tumor-Targeting Evaluation in vivo

To monitor the biodistribution and tumor-targeting ability of DPPs and A-DPPs in vivo, the 4T1 tumor-bearing Balb/c mice were randomly divided into 2 groups: A-DPPs group (Targeting group) and DPPs group (Non-targeting group). DiR-

labeled A-DPPs and DiR-labeled DPPs (4.0 mg/mL, 200 μL) were injected into mice through the tail vein, and in vivo fluorescence images were captured before and after injection at different time points (3, 6, 9, 24, 48 h) to detect the fluorescence signal intensity of the tumor sites. At 48 h after injection, the major organs (heart, liver, spleen, lung, kidney) and tumor tissues were dissected from each group for ex-vivo fluorescence imaging. The NIRF images of mice were obtained by the NightOWL LB 983 Living Animal Imaging System (Berthold, Germany). Furthermore, both DiI-labeled nanocomposites were injected into tumor-bearing mice via tail vein. Mice were sacrificed and dissected at 24 h post-administration. The collected tissues and organs were frozen and stained with DAPI and analyzed by CLSM.

Phase Transition and in vitro/vivo US Imaging Assessment

To test the thermal-responsive liquid-gas phase transition of A-DPPs, 20.0 μL of A-DPPs (4.0 mg/mL) was placed on the glass slide and heated. Optical images of nanoparticles were taken before and after 30s of heating at 60°C, 80°C and 90°C, respectively. To determine whether FUS can trigger phase transformation of A-DPPs, images of NPs solutions were captured before and after stimulation by Focused Ultrasound Tumor Therapeutic System (Model-JC200, Chongqing Haifu Medical Technology Co., Ltd, Chongqing, China) at parameters 1.0 MHz, 80 W/cm^2 for 5 s via an optical microscope (Olympus, Canada). Additionally, the %EE of PFH was determined according to Mousnier's method and % LC was tested by evaporation method.[23,24]

The ultrasound-imaging performance of A-DPPs in vitro was evaluated. A-DPPs (4.0 mg/mL), Blank NPs (4.0 mg/mL) and saline control were placed in 1 mL Eppendorf tube and exposed by a FUS transducer, then transferred to 3% agarose gel (w/v) phantom and images were taken immediately under B-mode and contrast enhanced ultrasound (CEUS) mode by using MyLab 90 (Esaote, Italy). Subsequently, the corresponding average gray values within the region of interest (ROI) were quantitatively measured by software ImageJ (National Institutes of Health, USA).

To investigate the US imaging capability in vivo, the tumor-bearing mice in different groups were injected with 200 μL A-DPPs (4.0 mg/mL), 200 μL DPPs (4.0 mg/mL) and 200 μL saline separately through tail vein for the FUS exposure and CEUS imaging later. Based on fluorescence distribution of nanoemulsion in vivo at time points, tumor sites of mice were exposed by the FUS transducer (1.0 MHz, 80 W/cm^2, 5 s) 24 h later after transvenous injection. The US and CEUS images before and after exposure were obtained using an ultrasonic diagnostic apparatus (MyLab 90, Esaote, Italy).

ROS Generation in vitro

The capability of A-DPPs to produce ROS in 4T1 cells in vitro was measured by DCFH-DA (Beyotime Biotechnology, China). 4T1 cells (1×10^4) were grown in CLSM dishes at 37°C (5% CO_2) for 24 h. All cells were divided into 6 groups: Control, Free DOX, Free DOX+FUS, FUS alone, A-DPPs and A-DPPs+FUS groups. Then, a serum-free medium containing DCFH-DA (1000 μL, 1 μM) was added to the culture dish and cells were incubated for 25 min for reaction with DCFH-DA to generate the steady green fluorescence signals (DCF). Next, the dishes were rinsed thrice with serum-free media to eliminate redundant DCFH-DA probes. Then, free DOX, A-DPPs (the equivalent DOX concentration was 20.0 μg/mL) were introduced by replenishing the fresh culture medium for 2 h. Next, dishes in FUS, Free DOX+FUS and A-DPPs+FUS groups were exposed by FUS (1.0 MHz, 80 W/cm^2, 5 s). CLSM images of intracellular ROS were captured at 495 nm and 485 nm. Finally, the cells were harvested for each group were detected for fluorescence density detection by Flow Cytometry.

Synergistic Killing Effects in vitro

To detect the synergistic inhibitory effects of FUS combined with A-DPPs on 4T1 cells in vitro, the cell proliferation assay was performed by Flow Cytometry. For evaluation of apoptosis rates, all cells were inoculated in 6-well plates (1×10^6/ well) for 24 h and were divided into 6 groups: Blank control, Free DOX, DPPs, A-DPPs, FUS alone and A-DPPs +FUS groups. Then, serum-free medium was added to the blank control group and FUS group, respectively, and serum-free medium containing Free DOX, DPPs, A-DPPs (DOX concentration of 20.0 μg/mL) were added to the corresponding groups. After co-incubation for 4 h, the nanoparticles that were not taken up by cells were washed with serum-free media. Digestion was performed with 0.25% trypsin (without EDTA) for 3 min. After digestion was terminated, all groups were added with saline to prepare cell suspensions and transferred to 1.5 mL centrifuge tubes. Specifically, cell

suspensions in the FUS group and A-DPPs+FUS group were exposed with FUS (1.0 MHz, 80 W/cm^2, 5 s), followed by the centrifugation (1000 rpm for 5 min) and washing twice. Finally, 1×10^6 cells were re-suspended in saline for cell apoptosis assessment using an annexin V/propidium iodide (PI) staining kit (Beyotime Biotechnology, China) by Flow Cytometry (Beckman Coulter, Inc., USA). Furthermore, the corresponding qualitative analysis of the synergistic killing effect was performed by CLSM.

Inhibitory Effect on Cell Invasion in vitro

Transwell chambers assay was performed to investigate the synergistic effect on cell invasion in vitro. The matrigel was added to the upper chambers and allowed solidification overnight at 37°C. 4T1 cells were incubated in serum-free media for 24 h, then harvested and suspended in serum-free media. However, cells in the A-DPPs group and the A-DPPs+FUS group were immersed in the serum-free medium containing A-DPPs (DOX concentration of 20.0 μg/mL). The cell suspensions in the FUS group and the A-DPPs+FUS group were exposed with FUS (1.0 MHz, 80 W/cm^2,5 s). Afterward, the cells were seeded onto the upper Transwell chambers (Corning Costar, Corning, USA) in 200 μL of serum-free medium with a density of 2×10^5/mL, and 500μL of RPMI-1640 medium with 20% FBS was added to the lower chambers as a chemoattractant and cells were plated in the upper membrane. After 48 h of incubation, the medium on the top chambers was removed and the cells retained in the upper chambers were washed with a cotton swab. On the opposite, the cells on the lower chambers were fixed by 4% paraformaldehyde and stained with crystal violet (15min). For invasion rate calculation, the cells were counted five times in random fields per chamber under a microscope (DC 300F, Leica, Germany) at ×100 magnification. The invasion rate was calculated with the non-treated cells as control.

In vivo FUS/Chemo Synergistic Therapeutic Efficacy

When the tumor size reached 100–150 mm^3, 4T1 tumor-bearing Balb/c mice were randomly divided into 6 groups with the following treatments (n = 5): (1) Saline; (2) Free DOX; (3) DPPs; (4) A-DPPs; (5) FUS; (6) A-DPPs+FUS. All agents were mixed in 200 μL Saline. For the Free DOX group, the DOX dose in each injection was 1.5 mg/kg. For (3), (4), (6) groups, each mouse was injected with agents at concentration of 4.0 mg/mL via tail vein, respectively. For groups with FUS, the FUS exposure was conducted by the therapeutic FUS transducer at an energy of 80 W/cm^2 for 5 s under a real-time guidance of diagnostic US imaging. The tumor volume and body weight of each mouse were measured every 3 days for 15 days, and tumor volume was calculated as follows: Tumor Volume (mm^3) = (Length × Width^2)/2. In addition, these mice were sacrificed 15 days after treatment and tumors of mice were harvested for H&E staining to observe apoptosis and necrosis, followed by TUNEL assay kit (Solarbio, China) staining. To determine the inhibition on metastasis by the combined therapeutic strategy, tumor tissues were conducted with the Vimentin immunohistochemistry assay. Additionally, treatments mentioned forehead were performed to explore the long-term (40 days) survival of mice bearing tumors. Survival probabilities were calculated as the percentage of mice that survived relative to the total mice in each group.

FUS Effects Enhanced by A-DPPs

To evaluate the FUS effects mediated by A-DPPs in vitro, the exposing procedure was conducted by Focused Ultrasound Tumor Therapeutic System (Model-JC200, Chongqing Haifu Medical Technology Co., Ltd, Chongqing, China) that mainly contains a therapeutic transducer (0.5–2 MHz of frequency and focal distance from 100 to 250 mm) for FUS, a real-time diagnostic transducer (3.5 MH of frequency) in the center of the therapeutic transducer for simultaneously monitoring therapeutic procedure and computer for automated control, individually. To examine the enhanced effect of FUS in vitro, fresh isolated bovine livers (10 cm × 10 cm × 10 cm in volume) were degassed for 1 h as the model in vitro, and were divided into 3 groups: A-DPPs, A-DPs and the saline control groups. Typically, 200 μL agents at 4.0 mg/mL were directly injected into the bovine livers by a 1 mL syringe, and the injection site was simultaneously monitored by a diagnostic US transducer in the FUS system. For each group, FUS was set at relative high energy (1.0 MHz, 100 W/cm^2, 5 s) and relative low energy (1.0 MHz, 80 W/cm^2, 5 s) for ablation on the injection sites. The volume of coagulated necrosis in liver tissues was calculated immediately after FUS according to the formula: V(mm^3) = (Length × Width^2)/2. Meanwhile, the passive cavitation of each exposure was recorded simultaneously via the passive cavitation detector (PCD) probe (National Instruments, USA) and the Energy Efficiency Factor (EEF) in each group was determined by the

formula: EEF (J/mm^3) =ηPt/V, where η represents the focusing coefficient of the transducer (η of JC-200 = 0.7); P is the total radiation sound power (W); T stands for the total exposure time (s); V equals the volume of coagulative necrosis (mm^3). Furthermore, grayscale value changes of coagulated liver tissues in each group before and after FUS exposure were recorded on the diagnostic ultrasound instrument to monitor synergistic FUS efficacy assisted by A-DPPs during FUS ablation.

Moreover, for the exploration into enhanced effects of FUS by A-DPPs in vivo, the tumor-bearing mice were injected by A-DPPs, A-DPs and saline via tail veins. Tumor regions were exposed by FUS (1.0 MHz, 80 W/cm^2, 5 s) monitored by US-imaging and PCD probe (National Instruments, USA) simultaneously at 24 h post administrations. After the mice were euthanized at Day 1, tumors and main organs were collected. Then the volumes of coagulative necrosis in tumors were stained with TTC assay kit and calculated according to the law: V(mm^3) = (Length × Width^2)/2. Meanwhile, the EEF in each group was determined by the formula: EEF (J/mm^3) =ηPt/V. Additionally, tumor tissues were conducted with H&E staining procedure for histological evaluation.

Statistical Analysis

All data were expressed as mean ± standard deviation (SD) and statistical analysis was performed using GraphPad Prism version 8.00 for Windows (GraphPad Software; La Jolla, CA, USA). Significant differences among groups were analyzed using a one-way ANOVA and differences for individual groups were determined using Student's *t*-test. The results were regarded as a significant difference when $*P < 0.05$. $**P < 0.01$, $***P < 0.001$.

Results and Discussion

Design, Synthesis and Characterization of AS1411-DOX/PFH-PEG@PLGA Nanoparticles

The multifunctional AS1411-DOX/PFH-PEG@PLGA nanoparticles (A-DPPs) were fabricated in a combination of double emulsion method followed with carbodiimide method to simultaneously encapsulate hydrophilic DOX and inert PFH as the core of the nanoparticles and link with AS1411 aptamer around the PLGA shell, as shown in Scheme 1. A-DPPs were elaborately designed to combine multiple functions, including active tumor targeting, ultra-sensitivity real-time US imaging and synergistic FUS ablation and chemotherapy on TNBC.

The physicochemical properties and morphology of the fabricated formulations were summarized in Table 1 and Figure 1. The A-DPPs displayed a uniform size and a consistent core-shell sphere under TEM observation (Figure 1A). The average diameter of the A-DPPs was 306.03±5.35 nm (PDI = 0.033±0.035), which was not significantly increased compared with DPPs (263.0 ± 1.16 nm). And the mean zeta potentials of A-DPPs were −4.05±0.13 mV while that of DPPs were −13.53 ± 0.40 mV (Figure 1B and C and Table 1). The favourable size and negative surface charge of NPs are conducive for NPs to escape absorption and elimination by the reticuloendothelial system and penetrate through the endothelial space of the tumor blood vessels based on passive enhanced permeability and retention (EPR) effect.[25,26] Moreover, the formation of a stable DNA (AS1411)-protein (nucleolin) complex depends on a negative binding energy, and a more negative binding energy corresponds to an increase in binding affinity.[27] Besides, the mean size and PDI value of A-DPPs remained relatively consistent in 10% fetal bovine serum medium at 37°C within seven days

Table 1 The Physical Characterizations of Nanoparticles

Nanoemulsion	Average Size (nm)	Zeta Potential (mV)	PDI	LC (%)	EE (%)
Blank NPs	189.33±3.35	−23.4 ± 0.96	0.054±0.046	–	–
A-DPs	258.83±12.77	−5.66 ± 0.49	0.046±0.006	3.86±0.1	30.90±0.76
DPPs	263.0 ± 1.16	−13.53 ± 0.40	0.057±0.041	5.29±0.03	42.28±0.26
A-DPPs	306.03 ± 5.35	−4.05 ± 0.13	0.033±0.035	3.53±0.39	29.33±3.38

Abbreviations: Blank-NPs, water-loaded PEG@PLGA nanoparticles; A-DPs, AS1411 aptamer modified DOX-loaded PEG@PLGA nanoparticles; DPPs, DOX-and-PFH-loaded PEG@PLGA nanoparticles; A-DPPs, AS1411 aptamer modified DOX-and-PFH-loaded PEG@PLGA nanoparticles; PDI, polydispersity index; LC, loading content of drug DOX; EE, encapsulation efficiency of drug DOX.

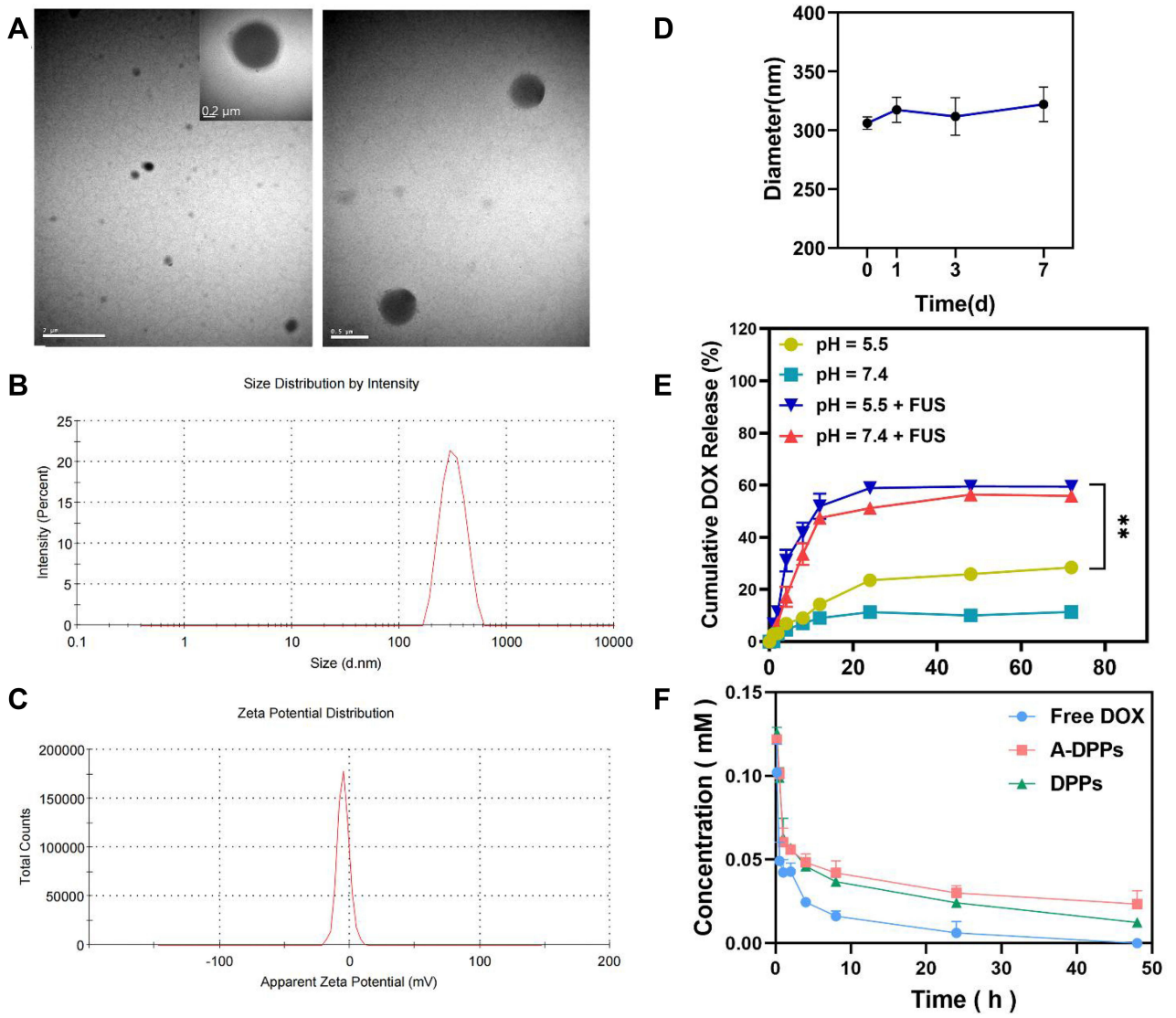

Figure 1 Physical and chemical characterization of the AS1411-DOX/PFH-PEG@PLGA NPs (A-DPPs). (**A**) TEM image of the A-DPPs (left scale bar=2 μm, middle scale bar=0.2 μm, right scale bar=0.5 μm). (**B**) The average size of A-DPPs. (**C**) The zeta Potential of A-DPPs. (**D**) The size distribution of A-DPPs in FBS within 7 days. The A-DPPs displayed a uniform size and negative zeta-potential with good bio-stability in vitro. (**E**) Cumulative DOX release at different pHs and FUS-exposure conditions was examined by UV-vis spectrophotometer. (**F**) The plasma pharmacokinetics of DOX from nanoparticles. The data were represented by mean±SD (n = 3). DOX released from A-DPPs was prolonged in vivo. $^{**}P < 0.01$.

(Figure 1D), which indicated the high stability of A-DPPs under simulative physiological conditions and the possibility of further in vivo study. The standard curve of DOX aqueous solution was drawn (Figure S1) and a linear equation underneath the concentration-absorbance intensity relationship was calculated as: $Y = 0.0178*X + 0.05081$ ($R^2 = 0.9972$), the DOX encapsulation efficiency (%EE) and loading content (%LC) of A-DPPs were 29.33±3.38%, 3.53±0.39%, respectively. In addition, the highest absorption peak of the A-DPPs overlapped with that of the drug, which indicated the successful packaging of anticancer drug DOX (Figure S2).

Then, the drug releasing behavior of A-DPPs triggered by FUS was measured by using the dialysis bag method. As shown in Figure 1E, an immediate dramatic drug release stimulated by FUS exposure was recorded in pH 5.5 (31.1 ±4.11%) and in pH 7.4 (17.21±3.87%) at the 4th h, and the sustained release of the drug within 72 hours was significantly higher than non-FUS exposure group, which demonstrated that DOX releasing behavior of A-DPPs could be triggered by FUS exposure. The acidic extracellular environment induced by glycolysis under hypoxic conditions is perhaps the most pervasive of tumor microenvironments.[28] We further explored the drug release of A-DPPs under different pH conditions, and the results showed that the drug release was higher at pH 5.5 than pH 7.4 regardless of US intervention, which may

be related to the higher dissolve ability of DOX in relation to a lower pH.[29] The pH-sensitive releasing pattern of A-DPPs can be controlled by the surrounding environment of TNBC.

Moreover, the drug release of A-DPPs in vivo and the pharmacokinetics of DOX in plasma were detected by UV−Vis spectrophotometry. After intravenous administration of certain doses of different DOX pharmaceutical, DOX was almost totally cleared from blood circulation within 24 h at a concentration of 0.006± 0.007 mM in Free DOX group, while the drug concentration in A-DPPs group was 5-fold higher than that at 0.03±0.004 mM (Figure 1F). The results showed that A-DPPs and DPPs were both stable in the blood circulation as time increased compared to free DOX, demonstrating that the nanocomposites had good physiological stability and a prolonged period of clearance.

Cytotoxicity and Biosafety Analysis in vitro and in vivo

The cytotoxicity of A-DPPs relative to free DOX against normal human hepatic L-O2 cells and murine TNBC 4T1 cells in vitro was examined by CCK-8 assay and the cell viability at varying corresponding DOX concentrations (1.25, 2.5, 5.0, 10.0, 20.0 and 40.0 μg/mL) is depicted in Figure 2. Figure 2A result revealed that the viability of hepatic L-O2 cells incubated with A-DPPs or DPPs was significant higher than that with free DOX ($P < 0.05$), which was consistent with

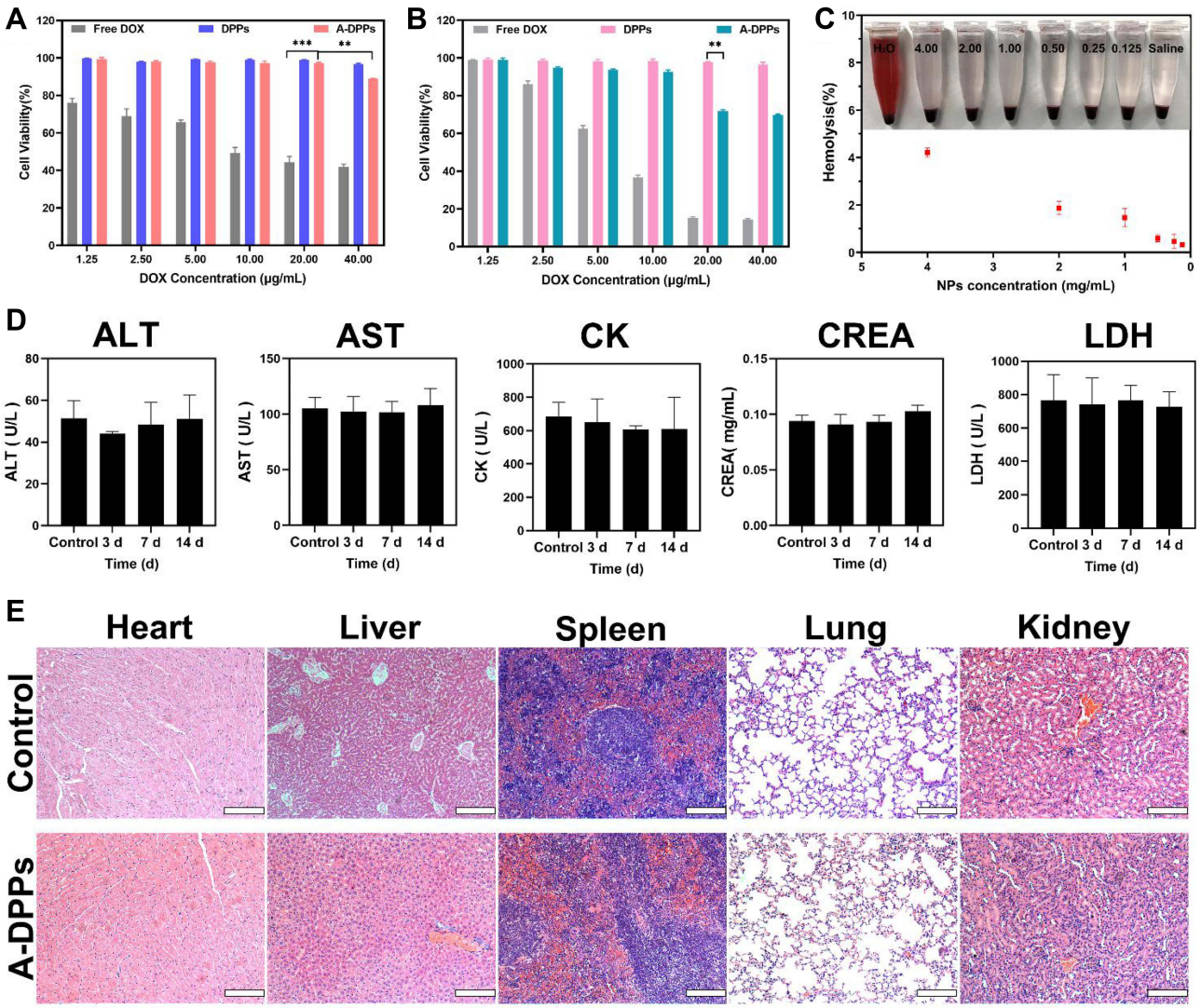

Figure 2 In vitro and vivo biosafety evaluation. Cell viability of free DOX, DPPs, A-DPPs on L-O2 human normal cells (**A**) and murine TNBC 4T1 cells (**B**) were measured by CCK-8 assay. The results showed that A-DPPs could inhibit 4T1 cells in a dose-dependent manner except for normal cells L-O2. (**C**) Hemolysis assays (n = 3). (**D**) Blood biochemistry analysis (n = 3). (**E**) H&E stained images of major organs of Balb/c mice post i.v. (scale bar = 200 μm). The results revealed that A-DPPs have a great biosafety in mice. $^{**}P < 0.01$, $^{***}P < 0.001$.

previous studies demonstrating that polymer shell-coated DOX nanoparticles exhibited high biocompatibility and desirable safety.[30,31] Whereas 4T1 cells' viability was declined to 71.74±0.82% distinctly with the co-culture of A-DPPs at the same 20.0 μg/mL concentration (Figure 2B), which may be because AS1411 is an anticancer aptamer that inhibits NF-κB signaling and down-regulates expression of bcl-2 to finally inhibit the cell viability of TNBC 4T1 cells.[32]

Since the nano emulsion needs to be delivered through blood, hemolysis assays are important to conduct the biosafety test for A-DPPs in vivo. As displayed in the Figure 2C, RBCs suspensions were incubated with A-DPPs at different concentrations (0.1, 0.25, 0.5, 1.0, 2.0, 4.0 mg/mL) and no obvious hemolysis phenomenon was observed. Even in highest concentration (4.0 mg/mL) of A-DPPs suspension, the hemolysis rate was less than 5%, which is considered as no-toxic according to ASTM F-756–08 standard.[33]

Moreover, we assessed the in vivo biosafety of A-DPPs by detecting the blood biochemical indices and pathological assessment of organ damage of rats. The blood chemical index analysis showed that alanine aminotransferase (ALT) and aspartate aminotransferase (AST) as liver function indicators, Creatinine (CREA) as renal function indicator and Creatine kinase (CK) and lactate dehydrogenase (LDH) as heart function indicators were no obvious differences compared to the saline control group values at 3, 7 and 14 days after A-DPPs injection (Figure 2D). Then, HE pathological assessment revealed no distinguished coagulative necrosis or injuries were found in major organs including heart, liver, spleen, lung and kidney at 14 day post injection of A-DPPs (Figure 2E), which re-confirmed that the biosafety of A-DPPs in vivo of biomedical applications. The lower toxicity of DOX-loaded nanoparticles could be due to the fact that the drug release characteristics exhibited the gradual release of DOX for a longer duration from nanoparticle formulation.[34]

In vitro Targeting Efficiency for 4T1 Cells

Before evaluating the targeting capability of A-DPPs, the bonding rate and stability of AS1411 aptamer linked to the surface of nanoparticles were firstly measured. Based on the CLSM, the overlap of green fluorescence (FAM modified aptamers) and red fluorescence (DiI-labeled NPs) was distinctively observed in the A-DPPs group while no significant overlap was displayed in the control (DPPs) group (Figure 3A). Meanwhile, the Flow Cytometry detected the combination rate of aptamer on A-DPPs (81.58±2.30%) was significantly higher than that on DPPs (0.70±1.17%) (Figure 3B), indicating that the A1411 aptamer was successfully and efficiently bond to the nanoparticles.

Then, we assessed the in vitro targeting efficiency of A-DPPs by CLSM and Flow Cytometry as shown in Figure 3C and D. After 4 h co-incubation, abundant DiI-labeled A-DPPs accumulated around and within the 4T1 cells while hardly non-target DPPs gathered around the cells, and there is almost no red fluorescence signal around the human normal L-O2 cells after co-incubation with targeting DiI-labeled A-DPPs, which indicated that DiI-labeled A-DPPs could not target towards into the normal cells around which nucleolin is not over-expressed. Nucleolin, one of the most abundant non-ribosomal phosphoproteins of nucleolus, is higher expression on rapidly proliferating cells including various cancer cells, which is related with the malignancy of cancers.[35–37] Besides, the quantitative result of targeting connection rate by Flow Cytometry in targeted A-DPPs group was 94.74±1.78%, substantially higher than that in non-targeted DPPs group (9.5±4.1%) and negative control L-O2 group (7.57 ±1.97%). The results showed that A-DPPs targeting capability is expected to achieve targeted accumulation in tumors as an aid in cancer imaging and therapy.

Biodistribution and Tumor-Targeted Ability of A-DPPs in vivo

To more precisely validate the tumor targeting accumulation and distribution of A-DPPs nanocomposites in vivo, DiR-labeled A-DPPs and DiR-labeled DPPs were injected into 4T1 tumor-bearing mice transvenously and the fluorescence images were taken and fluorescence signal intensity was detected at different time points. After 3 h of intravenous injection, the fluorescence distribution of the DiR-labeled NPs in mice was detected by Living Animal Imaging System (Figure 4A). The fluorescence intensity in the targeted group was gradually increased as time increased and reached a peak value at 24 h post-injection. Importantly, as time increased to 24 h post-injection, the fluorescence intensity of the targeted A-DPPs nanoparticles retained continuously increasing at tumor site. Comparatively, in the non-targeted DPPs group, the fluorescence intensity was all along significantly lower than that in the targeted group (Figure 4B). Afterwards, the frozen section of the tumor displayed abundant nanoparticles with red fluorescence signals in the targeting A-DPPs

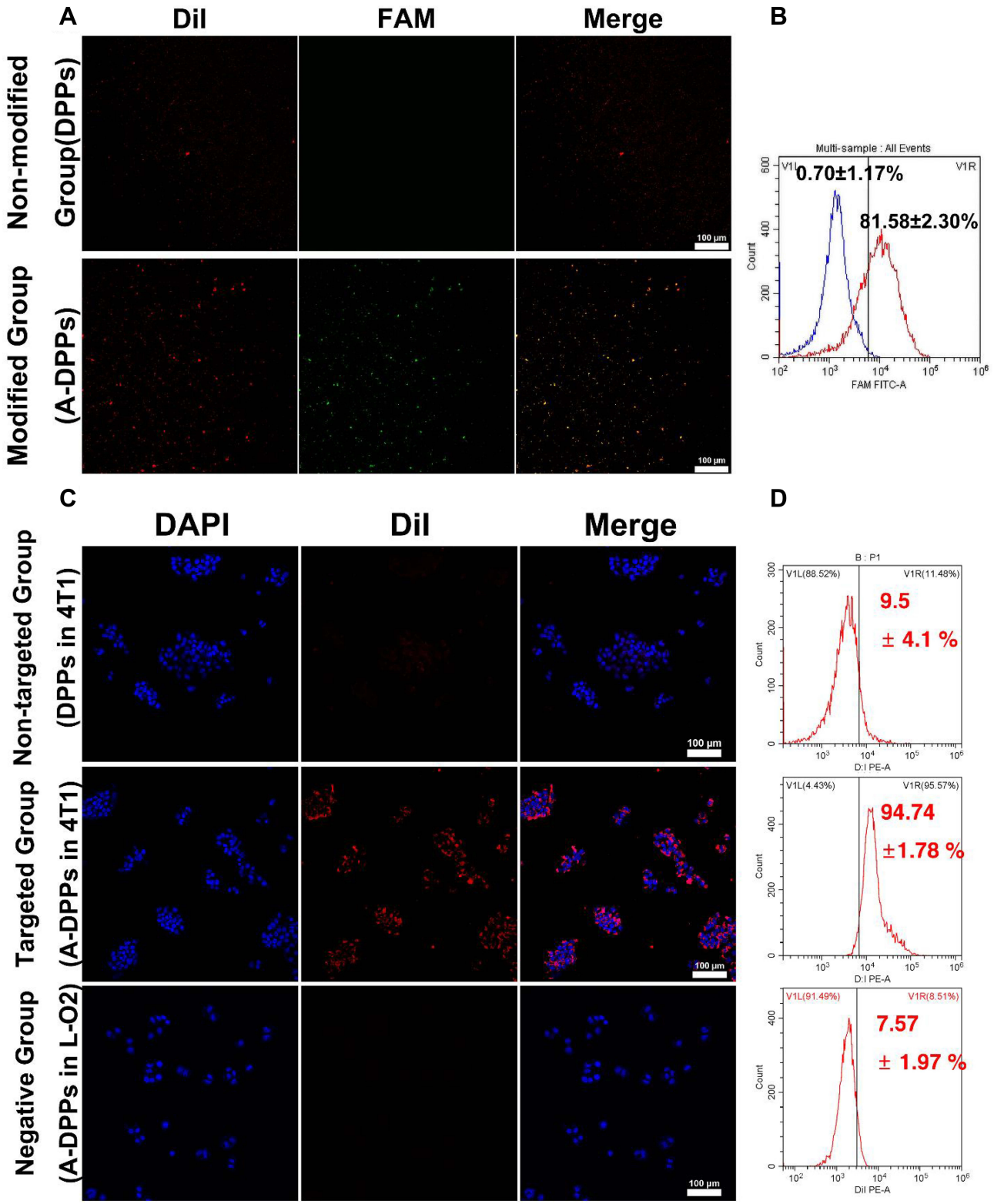

Figure 3 In vitro targeting ability of A-DPPs. (**A**) The conjugation of AS1411 aptamer with DPPs verified by CLSM and (**B**) the combination rate by flow cytometry. (**C**) Fluorescence signals in negative group (A-DPPs in L-O2 cells), non-targeted group (DPPs in 4T1 cells) and targeted group (A-DPPs in 4T1 cells) by CLSM (scale bar = 100 μm). (**D**) Cellular uptake of negative group, non-targeted group and targeted group by Flow Cytometry.

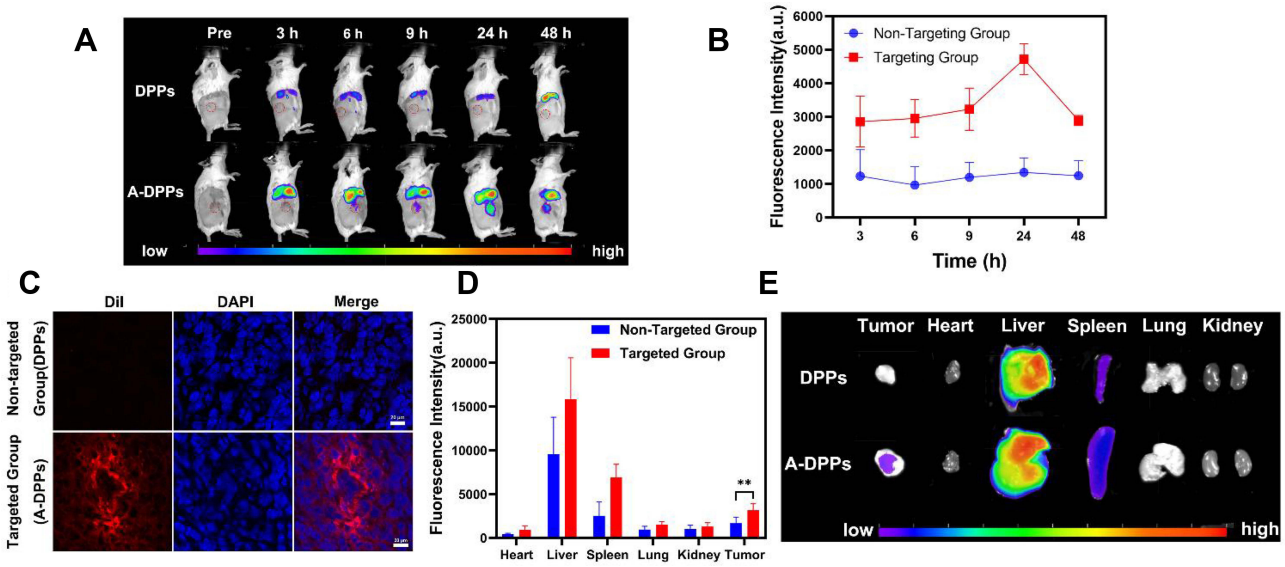

Figure 4 In vivo A-DPPs targeting and distribution. (**A**) Fluorescence intensity images of tumor-bearing Balb/c mice after being intravenously injected with DPPs and A-DPPs respectively at pre i.v., 3 h, 6 h, 9 h, 24 h and 48 h (n = 3). (**B**) Average fluorescence intensity of tumor sites for 48 hours. (**C**) The CLSM of tumor slices at 24 h after i.v. (scale bar = 20 μm). (**D**) Average fluorescence intensity histogram and (**E**) fluorescence intensity images of tumors and major organs isolated at 48 h post i.v. (n = 3). The data were represented by mean±SD. $^{**}P < 0.01$.

group but no small red signals were found in the non-targeting group DPPs at the same time (Figure 4C), further demonstrating the high targeting efficacy of A-DPPs nanoparticles.

In addition, the major organs (heart, liver, spleen, lung, kidney) and tumors were harvested at 24 h post-injection to further evaluate the ex vivo distribution of A-DPPs nanoparticles. As shown in Figure 4C, DOX was found to be distributed widely and rapidly into various organs (heart, liver, spleen, kidney, lung and tumor) after intravenous administration and the higher fluorescence signals were found in the liver and spleen, ascribed to the uptake effect of reticuloendothelial system.[38] The quantitative fluorescence intensity in the excised tumor of the A-DPPs injected group was 4723.87± 455.76 (a.u.), which was 3.5-fold ($P < 0.05$) higher than that in the non-targeted DPPs group of 1345.08 ±428.86 (a.u.) (Figure 4D). The above results demonstrated that the A-DPPs nanoparticles could actively and specially accumulate into tumor site due to the A1411 aptamer–nucleolin interaction, which lays a foundation for the imaging and treatment of tumors.

Phase Transformation and Performance of US Imaging in vitro and in vivo

The temperature-induced phase transition was explored at first. As displayed in Figure 5A, there were no microbubbles (MBs) enough to observe before heating. Compared to a few of them at 60°C, more MBs were swelled from A-DPPs at 80°C. As the temperature rose to 90°C, only several MBs were captured, which is consistent to the fact that vaporization of PFH balloon nanoparticles and let them burst.[39] The FUS-induced phase transformation was also conducted by using an optical microscope before and after FUS exposure on A-DPPs suspensions. A series of MBs emerged substantially after FUS exposure (Figure 5A), indicating that FUS could generate thermal effect and then trigger PFH vaporization inside nanoparticles. Moreover, the loading content of PFH was calculated to be 9.15 ± 0.67% and the encapsulation efficiency was 21.46 ± 1.85% (Table S1 and Figure S3).

The US imaging ability of nanoparticles in vitro was evaluated by FUS exposure on A-DPPs suspension, Blank NPs suspension and saline, respectively. Compared with the Blank NPs group and control group, the average grey value in ROI was significantly higher in A-DPPs group (47.56±3.65), which displayed the great US imaging performance of the nanocomposites (Figure 5B and C). PFH is a hydrophobic but highly biocompatible fluorocarbon compound with a low boiling point (≈56°C), which makes PFH more beneficial for FUS therapeutic monitoring of the tumor.[40] Due to the liquid-gas phase transition of PFH stimulated by the thermal effect of FUS, microbubbles from A-DPPs can perform as

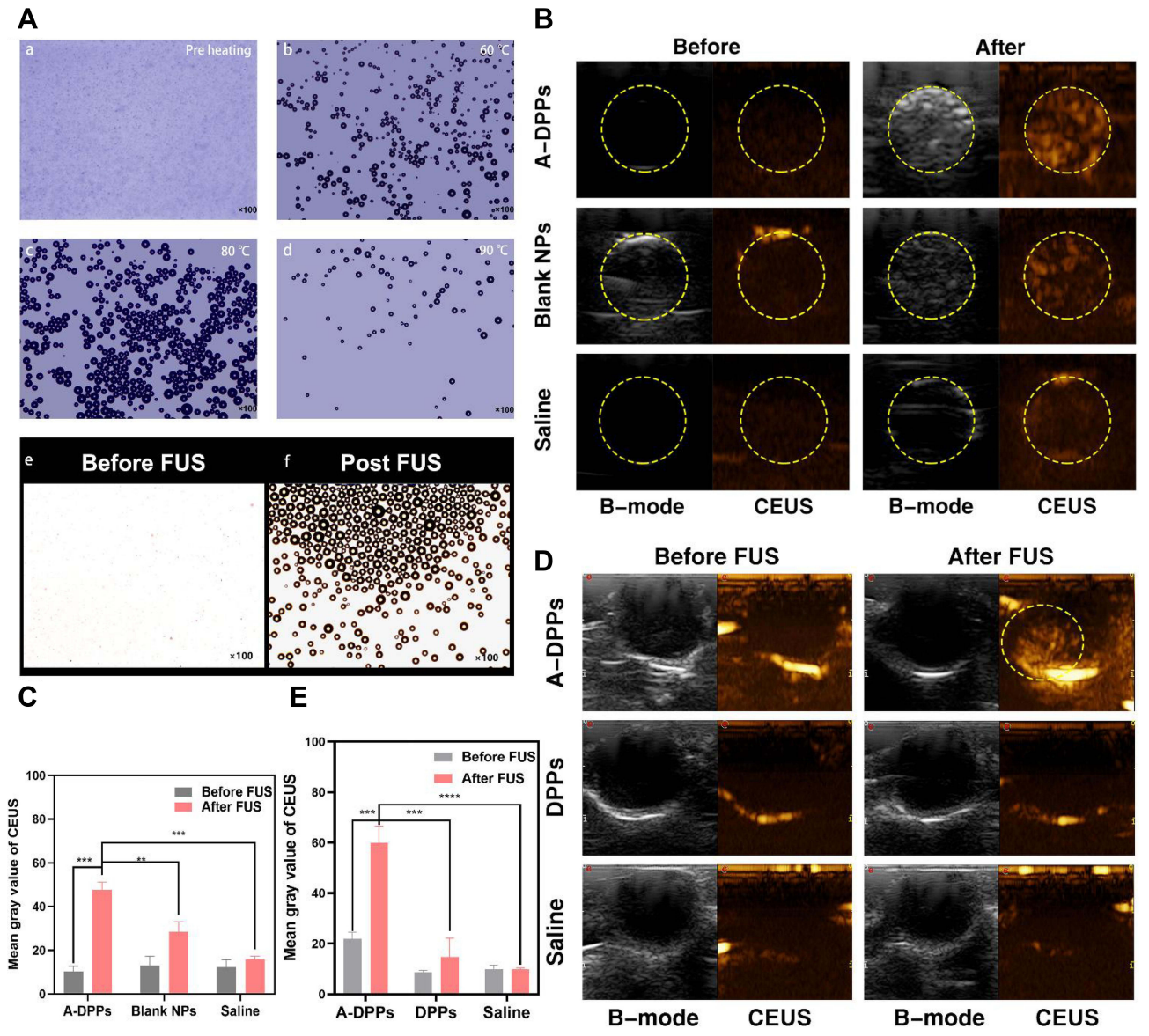

Figure 5 Phase transition of A-DPPs and US imaging in vitro and *vivo*. (**A**) Optical images of phase transition of A-DPPs heated at different temperatures (a: before heating, b: 60°C, c: 80°C, d: 90°C), and optical pictures of FUS-induced phase transformation of A-DPPs (e: before FUS, f: after FUS)(×100 magnification). (**B**) Gray level difference in B-mode and CEUS, and (**C**) Mean gray value of CEUS mode in ROI before and after FUS exposure in vitro. (**D**) CEUS mode images of ROI in tumor-bearing mice after intravenous injection of A-DPPs, DPPs and saline (n = 3). (**E**) Mean gray value of CEUS in tumor sites of different treatments before and after FUS exposure at 80 W/cm^2, 5 s. $^{**}P < 0.01$,$^{***}P < 0.001$,$^{****}P < 0.0001$.

additional cavitation nucleus to lower the threshold of cavitation effect of focused ultrasound.[41] This "small-to-big" strategy based on an elaborately designed temperature-responsive fluorocarbon nanoemulsion is anticipated to resolve the contradictions of synergistic agents size effect in FUS ablation surgery. In addition to the thermal effect of FUS, an optical droplet vaporization (ODV) process was recently realized for near infrared (NIR)-triggered vaporization of perfluorocarbon (PFC) liquid droplet. Comparatively, acoustic droplet vaporization (ADV) is an ideal strategy to realize the phase transformation of nanodroplets to form MBs for extravascular US imaging.[42]

Based on the results of US imaging ability of A-DPPs in vitro, the nanoparticles were injected in vivo as an imaging contrast agent. The B-mode and CEUS images were captured in three groups (A-DPPs, DPPs, Saline) during FUS treatment at 24 h post intravenous injection. The results indicated that the US imaging capability in vivo of A-DPPs could be boosted by FUS through liquid-gas phase transition of PFH (Figure 5D). The mean gray values under CEUS were significantly increased

in A-DPPs group (from 21.88±2.7 to 59.87±6.7) than that in DPPs group (from 8.66±0.78 to 14.7±7.42) and that in Saline group (from 9.9±1.56 to 9.81±0.62) (Figure 5E). The A-DPPs solution displayed a distinctly enhanced echo signal, which may be closely associated with the fact that FUS exposure stimulated PFH phase-transformation and caused nanospheres into microbubbles, producing strong backscattering echoes the principle of ultrasound imaging is mainly based on.[43] TNBC lacks of typical malignant US features of breast cancer, so early diagnosis and differential diagnosis of TNBC from other cancer types are facing great challenges.[44] However, targeting nano-scaled A-DPPs can accumulate tremendously in targeted tumor sites and their FUS-responsive phase transformation is sufficient to generate more intense backscattering signals in cases of diagnostic ultrasound for precise tumor targeted imaging.

Detection of ROS Generation in vitro

In the past two decades, numerous anti-tumor drugs have been used as sonosensitizers to evaluate their synergistic effects with ultrasound on different biological systems. Doxorubicin is one of the most studied anti-tumor drugs in SDT.[45] The CLSM observed that obvious green fluorescence was captured in free DOX or A-DPPs group after FUS sonication (Figure 6A), which indicated that DOX could generate ROS upon triggering by US and, thus, has the ability to kill tumor cells in SDT. Subsequently, quantitative analysis of ROS production shown in the A-DPPs+US group exhibited stronger fluorescence than other groups (Figure 6B and C). The reason may be related to the fact that nanoparticles can increase the acoustic cavitation effect and induce stronger sonochemical reactions to enhance the efficiency of ROS generation.[46] Investigation into the possible mechanisms revealed that sonodynamically induced reactive oxygen species and hydroxyl radical generation to result in DNA damage. ROS-mediated oxidative stress typically leads to oxidation of molecules and cell components, resulting in severe cellular damage, which is also important synergistic anticancer mechanisms in this study.[47,48]

In vitro Inhibition of Cell Proliferation and Invasion Analysis

The synergistic effect on cancer cells' proliferation and invasion by FUS combined with nanoparticles is crucial for treatment. In this study, 4T1 cells' apoptosis induced by FUS with A-DPPs was qualitatively detected by CLSM imaging

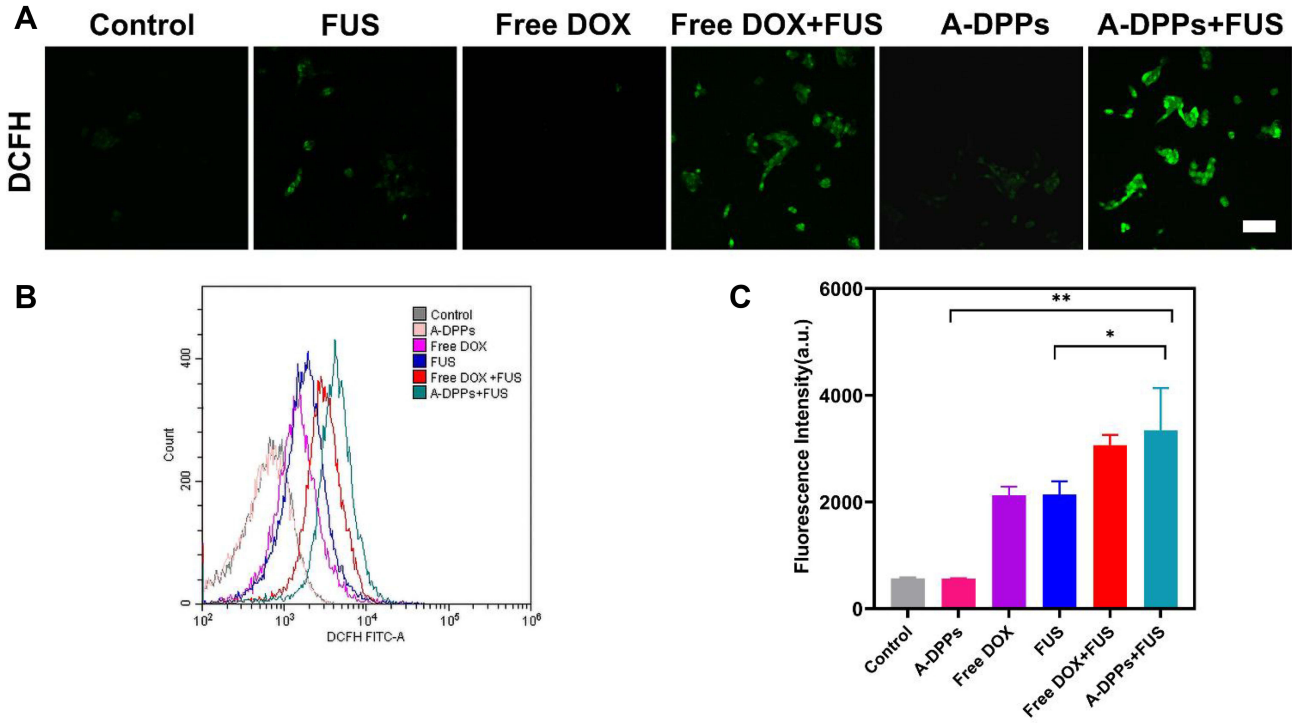

Figure 6 ROS production of A-DPPs with FUS in vitro. (**A**) Green fluorescence intensity of intracellular ROS production in cells captured by CLSM qualitatively and by flow cytometry (**B**) and (**C**) quantitative results. (scale bar = 100 μm). *$P < 0.05$, **$P < 0.01$.

and quantitatively by Flow Cytometry. The live and dead cells were marked by Calcein-AM (green fluorescence) and PI (red fluorescence) to observe under CLSM, and the live cell counts green fluorescence significantly declined after combined treatment of FUS and A-DPPs when compared with other treatments (Figure 7A and B). Moreover, the apoptosis rate of 4T1 cells was significantly higher in A-DPPs+FUS group (89.80±1.32%) compared to the single FUS or DOX treatment, which demonstrated that FUS combined with A-DPPs could product an obvious synergistic killing effect on 4T1 cells (Figure 7C). Additionally, the inhibitory effect on 4T1 cell invasion by FUS/chemo synergistic effect was further confirmed by transwell chamber assay, and the result demonstrated that the increased number of cell in transmembrane in A-DPPs+FUS (30.13±2.86%) group was less than that in FUS alone group (73.4±2.61%) and that in A-DPPs group (67.13±2.8%) (Figure 7D and E). These results indicated that synergistic FUS/chemotherapy can induce inhibitory effect on the proliferation and invasion of 4T1 cells.

Synergistic Therapeutic Effect of A-DPPs for FUS Ablation in vivo

To confirm the synergistic therapeutic effect of A-DPPs as a theranostic nanocomposite, the treatments combined with FUS and A-DPPs on Balc/c mice bearing TNBC were conducted in vivo as shown in Figure 8A. The tumor volumes and body weight in each group were measured every 3 days for 15 days post different treatments. The volume of tumors in the DPPs group (712.05±131.87 mm^3), Free DOX group (820.58±120.76 mm^3) was gradually increased for successive 15 days and higher than that in the control group (1539.86±471.44 mm^3), indicting no obvious anti-tumor effect of single free drug or non-targeted nanoparticles. However, the tumor size in the FUS group (592.9±51.30mm^3) and the A-DPPs

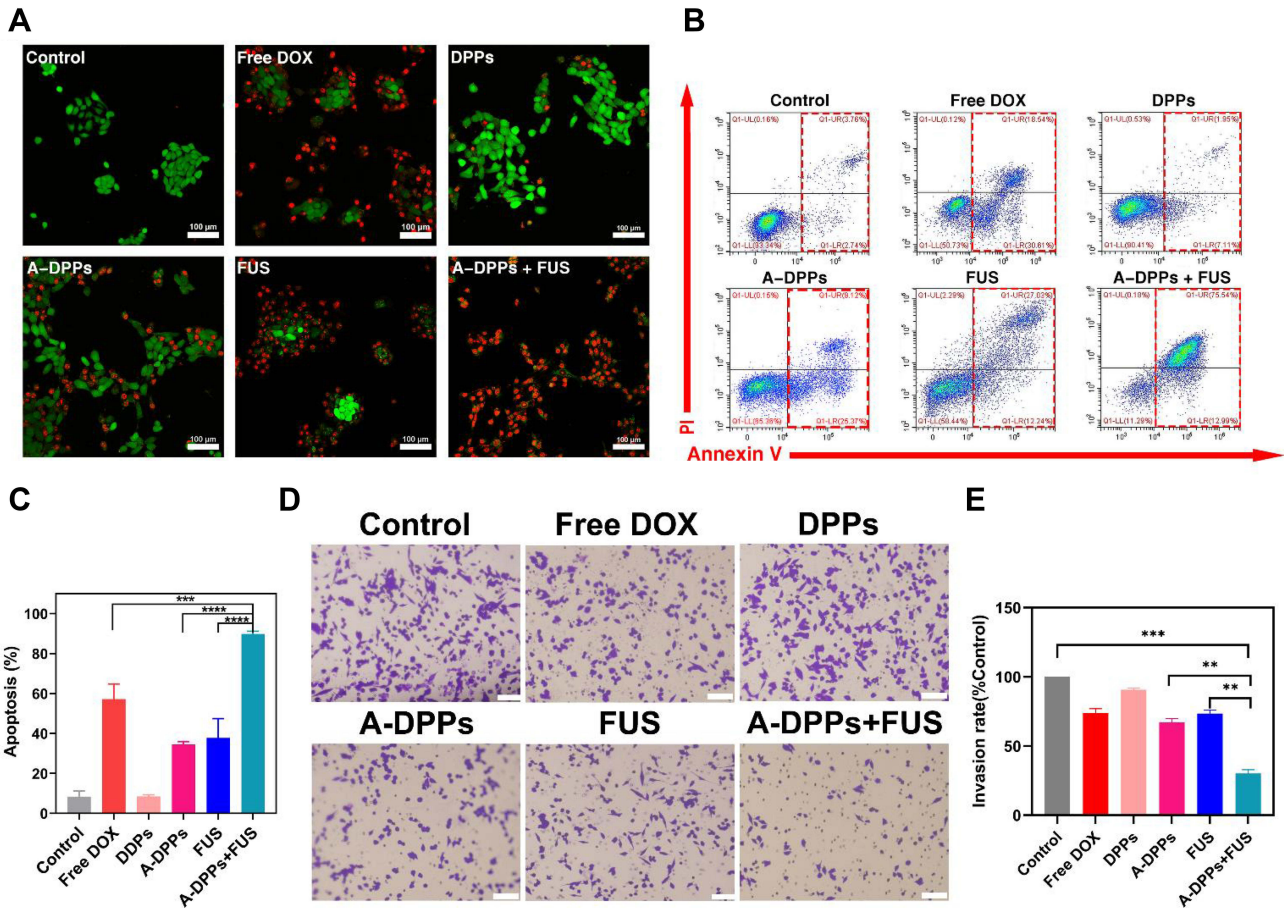

Figure 7 A-DPPs combined with FUS induce 4T1 cell apoptosis and inhibit cells invasion in vitro. (**A**) Confocal images of fluorescence signals by annexin V-PI staining in 4T1 cells (red: dead cells, green: live cells; scale bar =100 μm). Flow cytometric analysis of apoptosis in 4T1 cells using annexinV-PI staining (**B**) and quantitative results (**C**). The invasion of cells was determined by Transwell Chamber assay and results were represented in qualitatively (**D**) and quantitatively (**E**). The data were represented by mean ±SD. $^{**}P < 0.01$, $^{***}P < 0.001$, $^{****}P < 0.0001$.

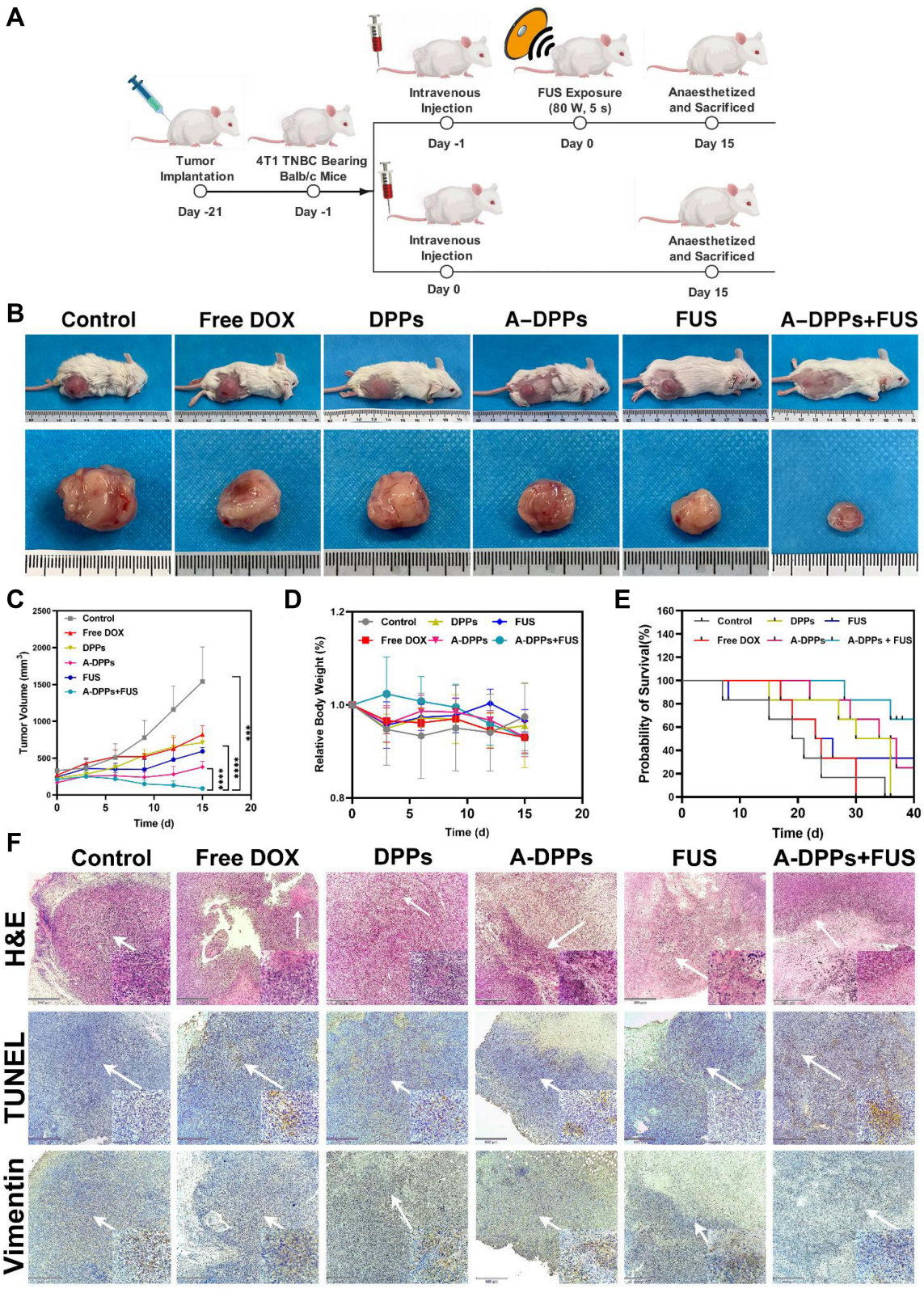

Figure 8 In vivo synergistic effects of A-DPPs mediated FUS/chemotherapy. (**A**) The illustration of therapy in tumor-bearing mice. (**B**) Digital photos of tumor-bearing mice and isolated tumors at Day 15 post different treatments. (**C**) Tumor volumes and (**D**) mice relative body weight in different treatments for successive 15 days (n = 4) for each group. (**E**) Survival curve of tumor-bearing mice after different therapies (n = 6). (**F**) H&E stained images and immunohistochemistry photos of tumors conducted by different treatments. The data were represented by mean±SD for each group. ***$P < 0.001$, ****$P < 0.0001$.

group (379.14±77.82mm^3) grew much slower and smaller. Comparatively, the tumor volumes after A-DPPs +FUS combined treatment were significantly decreased within 15 days, which indicated that FUS combined with A-DPPs had a distinguished tumor growth inhibition effect (Figure 8B and C and Figure 4). Moreover, relative body weights in every group were recorded during 15-day observation and no significant differences were found among all the groups (Figure 8D). More importantly, the survival probabilities curve showed that the mice in A-DPPs+ FUS group lived longer distinctly than other mice, demonstrating that the combined therapy could prolong the expectancy of tumor-bearing mice (Figure 8E).

Then, H&E staining, TUNEL staining were performed to evaluate the histological changes and tumor cell apoptosis. H&E-stained slices pictures directly displayed that A-DPPs+FUS caused remarkable substantial cell necrosis and destruction of the tumor cell nucleus, collapse of the cellular structure. Simultaneously, TUNEL-stained images revealed considerable induction of apoptosis and many apoptotic cells extensively distributed across tumor slices. For the evaluation of the inhibitory effect of the combined therapeutic strategy on the proliferation and potential metastasis, we detected the expression of Vimentin to explore the immunity in TNBC mice. Vimentin plays a crucial part in regulating epithelial–mesenchymal transition (EMT) which is a characteristic process associated with tumor invasion and metastasis in breast cancer cells.[49–51] The IHC assays revealed that the expression of Vimentin was decreased remarkably in tumor tissues in synergistic FUS/chemotherapy compared to other treatments (Figure 8F), which displayed that combinatorial FUS/chemo therapy may boost immune effects. Overall, the favorable prognosis may be attributed to the suppression on tumors' growth and formation of metastasis by effective anti-tumor immune responses triggered by synergistic FUS/chemo therapy.

Enhanced Thermal and Acoustic Cavitation Effect of A-DPPs Mediated FUS Ablation

To explore the mechanism of synergistic effect of A-DPPs for FUS ablation, we compared the ablation efficacy of A-DPPs and A-DPs (without PFH) mediated FUS treatment in isolated bovine liver and in vivo of tumor-bearing mice. After FUS ablation of isolated bovine liver or in vivo of tumor-bearing mice, the coagulative necrosis volume of A-DPPs group was significantly higher than that of A-DPs and saline control groups under the FUS exposure at 80 W/cm^2 for 5 s. When the ultrasound energy was raised to 150 W/cm^2 for 5 s, the coagulative necrosis volume in A-DPPs group was also the most obvious (Figure 9A and B). Moreover, the energy efficiency factor (EEF defined as the ultrasound energy delivered for 1 mm^3 of the coagulative necrosis in tissue) and gray level changes during treatment were considered to be the key factors to evaluate ablation effect.[52] The grayscale value difference after FUS in the A-DPPs group was significantly stronger than that in the A-DPs group under 80 W/cm^2 or 150 W/cm^2 for 5 s (Figure 9C and D). Meanwhile, EEF in the A-DPPs group was significantly lower than that in the other groups (Tables 2 and 3), indicating that A-DPPs could improve the ablation efficiency of FUS and enhanced the ultrasound signals under the same exposure parameters (Figure 9E–H).

Furthermore, the cavitation effect prompted by A-DPPs during the FUS exposure was detected via passive cavitation signals from the PCD probe. The broadband noise generated during FUS was characteristic spectra of inertial cavitation.[53] The result showed that signal amplitude values were apparently higher in A-DPPs group than in A-DPs during the 80 W/cm^2 and 150W/cm^2 exposure, respectively, in isolated bovine liver and in vivo of tumor-bearing mice, suggesting that the introduction of PFH inside the A-DPPs nanocomposites could change the acoustic environment and boost the cavitation effect of FUS, for which more cavities on the ablated areas in A-DPPs group were produced and the threshold of cavitation was reduced (Figure 9I–K).[54] It holds to previous studies that contrast agents were deemed to change the acoustic characteristics of the tissue, enhance the deposition of FUS energy and promote the cavitation in the targeted sites.[55] Additionally, H&E staining results displayed that cell damage was mainly characterized by cell pyknosis, nuclear pyknosis with heavy staining, significantly widened cell gaps, and intact cellular contours. The coagulative necrosis areas were remarkably enhanced in joint FUS/chemo therapeutic strategy (Figure 9L). It may be related to the fact that inertial cavitation prompted by A-DPPs can enhance heating at the focus, increase chemotherapeutic potency, elevate mechanical and, more importantly, biological effects of FUS.[56–58]

As for the biological effects, bubble collapse by cavitation can generate shock waves and micro-jets near the boundary that can lead to cell damage via sonomechanical effect.[59] Simultaneously, ROS is also produced by inertial cavitation through sonochemical effect.[60,61] Intracellular ROS in SDT can cause ultrastructural damage and the

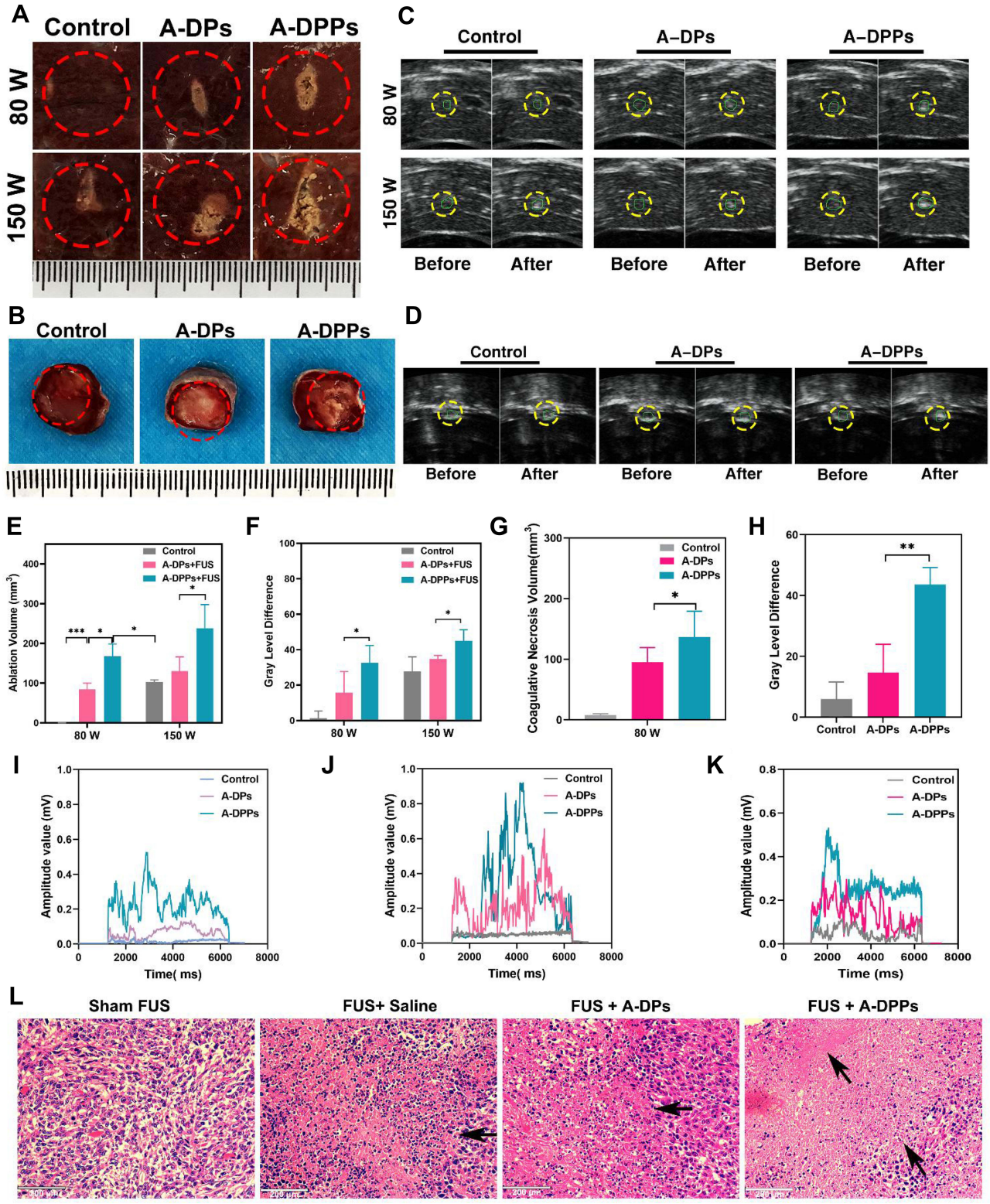

Figure 9 In vitro and vivo enhanced thermal effect and acoustic cavitation effect of FUS assisted by A-DPPs. (**A**) Digital photos of ablated areas in vitro fresh bovine livers after the injection of A-DPPs, A-DPs, and saline, followed by FUS exposure (80 W/cm^2, 5 s and 150W/cm^2, 5 s). (**B**) Photos of coagulative necrosis in tumor-bearing mice in vivo at FUS parameter (80 W/cm^2, 5 s). (**C**) Real-time Ultrasound images in bovine livers before and after FUS exposure (80 W/cm^2, 5 s and 150 W/cm^2, 5 s) and (**D**) in tumor sites prior and post FUS (80 W/cm^2, 5 s). (**E**) Volumes of coagulative necrosis and (**F**) grayscale value difference of ROI in bovine livers. (**G**) Volumes of coagulative necrosis and (**H**) grayscale value difference of ROI in tumor-bearing mice. The passive cavitation signals of different treatments in bovine livers at 80 W/cm^2 (**I**) and 150 W/cm^2 (**J**) for 5 s and in vivo mice at 80 W/cm^2 for 5 s (**K**). (**L**) Histological changes of tumor sites by different treatments after 24 h of FUS exposure were performed by H&E staining. The ablated volume was larger and cavitation signals were stronger in the A-DPPs group than that in other groups after FUS exposure at the same condition. Necrosis was distinct in the A-DPPs group such as cell pyknosis, nuclear pyknosis with heavy staining, widened cell gaps, and intact cellular contours. The data were represented by mean±SD (n = 3) for each group. *P < 0.05, **P < 0.01, ***P < 0.001.

Table 2 Comparison of FUS EEF in Fresh Bovine Livers in vitro

Groups	EEF (J/ mm^3)	
	80 W/cm^2 FUS	150 W/cm^2 FUS
Saline	–	5.11 ± 0.27
A-DPs	3.41 ± 0.72	4.23 ± 1.12
A-DPPs	1.45 ± 0.20#	1.93 ± 0.05#*
P	<0.01	<0.01

Notes: #Represents statistically significant difference with 150W/cm^2 FUS + Saline group, $P < 0.05$. *Represents statistically significant difference with 150W/cm^2 FUS + A-DPs group, $P < 0.05$.

Table 3 Comparison of FUS EEF in Tumors in vivo

Groups	EEF (J/ mm^3)
Saline	39.0 ± 10.51
A-DPs	3.09 ± 0.85
A-DPPs	1.66 ± 0.14#
P	<0.01

Note: #Represents statistically significant difference with FUS + Saline group, $P < 0.05$.

cytoskeletal component destruction in cells, which is relevant to the vimentin.[62] Moreover, the focused ultrasound can mediate anti-tumor immune responses.[63–65] Thus, in our studies, the mechanism of the favorable prognosis may be attributed to the fact that combinatorial FUS/chemo therapy can reduce EMT with assistance of SDT and DOX through the cavitation effects, thermal effects and biological effects of FUS.[66,67] However, the molecular mechanism remains unclear, which is worth more intense researches in future.

Multi-modal combined theranostic strategy is the trend of tumor therapy in modern medicine. Nano-ultrasonic biomedicine, as a special cross-disciplinary research frontier, can overcome the drawbacks of traditional microbubbles and utilize novel US-based contrast agents or synergistic agents for noninvasive therapeutic modalities with high efficiency and negligible side effects.[68] In this study, we fabricated a multifunctional theranostic nanoparticles of A-DPPs for enhanced tumor targeted imaging and synergistic FUS ablation and chemotherapy on TNBC. After exposure to FUS exposure, the A-DPPs exhibited liquid-gas phase transition and repeatedly enhanced tumor targeted imaging and FUS-ablation efficacy post a single intravenous administration. In addition to the nano-ultrasonic multifunctional synergistic agents for FUS-based cancer ablation surgery, the elaborate design of magnetic resonance (MR) or photoacoustic (PA)-guided micro/nanoparticles also realizes some intriguing chemotherapy or radiotherapy.[69,70] Compared to the MR or PA-guided micro/nanoparticles for multi-modal therapy, FUS-mediated integration of diagnosis and therapy is regarded as one of the most promising approaches due to its unique nature of deep tissue-penetration, non-ionizing technique for precise acoustic energy deposition into tissues, real-time monitoring and easy manipulation.[71] Importantly, the immunological responses triggered by multi-modal non-invasive FUS thermal ablation surgery may provide a refreshing perspective into the combined FUS/immunotherapy in the future.[72]

Conclusion

In this study, we describe a newly developed nanosized theranostic agent, AS1411-DOX/PFH-PEG@PLGA nanoparticles (A-DPPs), which was fabricated using AS1411 aptamer-conjugated and DOX/PFH encapsulated PEG@PLGA NPs. The A-DPPs exhibited excellent tumor targeted US imaging properties via phase-transformation of PFH and pH/US dual sensitive release properties, which enhanced the chemotherapeutic effect and sonication-induced hyperthermia under

FUS exposure. Furthermore, the synergistic DOX chemotherapy and FUS therapy and SDT effect could overcome the limitations of a single therapy and enhance the treatment efficiency on triple negative breast cancer. The synergistic mechanism may be that the combined therapy of FUS and A-DPPs enhances the ultrasonic cavitation effect and thermal effect, and effectively triggered biological effects. Our results indicate that the multifunctional A-DPPs nanocarriers together with the SDT and FUS synergistic therapy could be used in new approaches for triple negative breast cancer therapy.

Abbreviations

TNBC, Triple negative breast cancer; FUS, focused ultrasound; SDT, sonodynamic therapy; PFH, Perfluorohexane; DOX, Doxorubicin; UCA, ultrasound contrast agent; ROS, reactive oxygen species; EEF, energy efficiency factor; ER, estrogen receptor; PR, progesterone receptor; HER2, human epidermal growth factor receptor 2; NPs, nanoparticles; CEUS, contrast enhanced ultrasound; US, ultrasound; PLGA, poly (lactic-co-glycolic acid); PEG, Poly(ethylene glycol); EPR, enhanced permeability and retention; $CHCI_3$, Chloroform; PVA, Polyvinyl alcohol; DiI, 1,1-dioctadecyl-3,3,3′,3′-tetramethylindocarbocyanine perchlorate; DAPI, 4’,6-diamidino-2-phenylindole; EDC, 1-ethyl-3-(3-dimethylaminopropyl) carbodiimide; NHS, N-hydroxysuccinimide; DiR, 1,1′-dioctadecyl-3,3,3′,3′-tetramethylindotricarbocyanineiodide; DCFH-DA, 2,7-dichlorodihydrofluorescein diacetate; OD, optical density; PDI, polydispersity index; TEM, Transmission electron microscopy; LE, Loading efficiency; EE, encapsulation efficiency; H&E, hematoxylin and eosin; CLSM, confocal laser scanning microscopy; ALT, alanine aminotransferase; AST, aspartate transaminase; TBIL, total bilirubin; CREA, Creatinine; CK, Creatine kinase; LDH, lactate dehydrogenase; TUNEL, terminal deoxynucleotidyl transferase-mediated dUTP-biotin nick end labeling.

Disclosure

The authors report no conflicts of interest in this work.

References

1. Siegel RL, Miller KD, Jemal A. Cancer statistics, 2020. *CA Cancer J Clin*. 2020;70(1):7–30. doi:10.3322/caac.21590
2. Waks AG, Winer EP. Breast cancer treatment: a review. *JAMA*. 2019;321(3):288–300. doi:10.1001/jama.2018.19323
3. Bianchini G, Balko JM, Mayer IA, Sanders ME, Gianni L. Triple-negative breast cancer: challenges and opportunities of a heterogeneous disease. *Nat Rev Clin Oncol*. 2016;13(11):674–690. doi:10.1038/nrclinonc.2016.66
4. Duc NM, Keserci B. Emerging clinical applications of high-intensity focused ultrasound. *Diagn Interv Radiol*. 2019;25(5):398–409. doi:10.5152/dir.2019.18556
5. Ning Z, Xie J, Chen Q, et al. HIFU is safe, effective, and feasible in pancreatic cancer patients: a monocentric retrospective study among 523 patients. *Onco Targets Ther*. 2019;12:1021–1029. doi:10.2147/OTT.S185424
6. Orgera G, Monfardini L, Della Vigna P, et al. High-intensity focused ultrasound (HIFU) in patients with solid malignancies: evaluation of feasibility, local tumour response and clinical results. *Radiol Med*. 2011;116(5):734–748. doi:10.1007/s11547-011-0634-4
7. You Y, Wang Z, Ran H, et al. Nanoparticle-enhanced synergistic HIFU ablation and transarterial chemoembolization for efficient cancer therapy. *Nanoscale*. 2016;8(7):4324–4339. doi:10.1039/C5NR08292G
8. Ektate K, Munteanu MC, Ashar H, Malayer J, Ranjan A. Chemoimmunotherapy of colon cancer with focused ultrasound and Salmonella-laden temperature sensitive liposomes (thermobots). *Sci Rep*. 2018;8:13062.
9. Wilson K, Homan K, Emelianov S. Biomedical photoacoustics beyond thermal expansion using triggered nanodroplet vaporization for contrast-enhanced imaging. *Nat Commun*. 2012;3(1):618. doi:10.1038/ncomms1627
10. Li DS, Kripfgans OD, Fabiilli ML, Brian Fowlkes J, Bull JL. Initial nucleation site formation due to acoustic droplet vaporization. *Appl Phys Lett*. 2014;104(6):063703. doi:10.1063/1.4864110
11. Hu CM, Zhang L. Nanoparticle-based combination therapy toward overcoming drug resistance in cancer. *Biochem Pharmacol*. 2012;83(8):1104–1111. doi:10.1016/j.bcp.2012.01.008
12. Tacar O, Sriamornsak P, Dass CR. Doxorubicin: an update on anticancer molecular action, toxicity and novel drug delivery systems. *J Pharm Pharmacol*. 2013;65(2):157–170. doi:10.1111/j.2042-7158.2012.01567.x
13. Maeda M, Muragaki Y, Okamoto J, et al. Sonodynamic therapy based on combined use of low dose administration of epirubicin-incorporating drug delivery system and focused ultrasound. *Ultrasound Med Biol*. 2017;43(10):2295–2301. doi:10.1016/j.ultrasmedbio.2017.06.003
14. Zhu ZF, Chen LJ, Lu R, et al. Tripeptide tyroserleutide plus doxorubicin: therapeutic synergy and side effect attenuation. *BMC Cancer*. 2008;8(1):342. doi:10.1186/1471-2407-8-342
15. Pawar A, Prabhu P. Nanosoldiers: a promising strategy to combat triple negative breast cancer. *Biomed Pharmacother*. 2019;110:319–341. doi:10.1016/j.biopha.2018.11.122
16. Cabeza L, Ortiz R, Arias JL, et al. Enhanced anti-tumor activity of doxorubicin in breast cancer through the use of poly(butylcyanoacrylate) nanoparticles. *Int J Nanomed*. 2015;10:1291–1306.

17. Wang Q, Zhong Y, Liu W, et al. Enhanced chemotherapeutic efficacy of the low-dose doxorubicin in breast cancer via nanoparticle delivery system crosslinked hyaluronic acid. *Drug Deliv*. 2019;26(1):12–22. doi:10.1080/10717544.2018.1507057
18. Danhier F, Ansorena E, Silva JM, Coco R, Le Breton A, Preat V. PLGAbased nanoparticles: an overview of biomedical applications. *J Controlled Release*. 2012;161(2):505–522. doi:10.1016/j.jconrel.2012.01.043
19. Barbas AS, Mi J, Clary BM, White RR. Aptamer applications for targeted cancer therapy. *Future Oncol*. 2010;6(7):1117e26. doi:10.2217/fon.10.67
20. Soundararajan S, Chen W, Spicer EK, Courtenay-Luck N, Fernandes DJ. The nucleolin targeting aptamer AS1411 destabilizes Bcl-2 messenger RNA in human breast cancer cells. *Cancer Res*. 2008;68(7):2358–2365. doi:10.1158/0008-5472.CAN-07-5723
21. Soundararajan S, Wang L, Sridharan V, et al. Plasma membrane nucleolin is a receptor for the anticancer aptamer AS1411 in MV4-11 leukemia cells. *Mol Pharmacol*. 2009;76(5):984–991. doi:10.1124/mol.109.055947
22. Kong N, Deng M, Sun XN, Chen YD, Sui XB. Polydopamine-functionalized CA-(PCL-ran-PLA) nanoparticles for target delivery of docetaxel and chemo-photothermal therapy of breast cancer. *Front Pharmacol*. 2018;9:125. doi:10.3389/fphar.2018.00125
23. Mousnier L, Huang N, Morvan E, Fattal E, Tsapis N. Influence of polymer end- chemistry on the morphology of perfluorohexane polymeric microcapsules intended as ultrasound contrast agents. *Int J Pharm*. 2014;471(1–2):10–17. doi:10.1016/j.ijpharm.2014.05.012
24. Su YL, Fang JH, Liao CY, Lin CT, Li YT, Hu SH. Targeted mesoporous iron oxide nanoparticles-encapsulated perfluorohexane and a hydrophobic drug for deep tumor penetration and therapy. *Theranostics*. 2015;5(11):1233–1248. doi:10.7150/thno.12843
25. Björnmalm M, Thurecht KJ, Michael M, Scott AM, Caruso F. Bridging bio-nano science and cancer nanomedicine. *ACS Nano*. 2017;11 (10):9594–9613. doi:10.1021/acsnano.7b04855
26. Shi Y, van der Meel R, Chen X, Lammers T. The EPR effect and beyond: strategies to improve tumor targeting and cancer nanomedicine treatment efficacy. *Theranostics*. 2020;10(17):7921–7924. doi:10.7150/thno.49577
27. Davies MN, Sansom CE, Beazley C, Moss DS. A novel predictive technique for the MHC class II peptide-binding interaction. *Mol Med*. 2003;9(9–12):220–225. doi:10.2119/2003-00032.Sansom
28. Gatenby RA, Gillies RJ. Why do cancers have high aerobic glycolysis? *Nat Rev Cancer*. 2004;4(11):891–899. doi:10.1038/nrc1478
29. Unsoy G, Khodadust R, Yalcin S, Mutlu P, Gunduz U. Synthesis of doxorubicin loaded magnetic chitosan nanoparticles for ph responsive targeted drug delivery. *Eur J Pharm Sci*. 2014;62:243–250. doi:10.1016/j.ejps.2014.05.021
30. Li G, Li J, Hou Y, et al. Levofloxacin-loaded nanosonosensitizer as a highly efficient therapy for bacillus Calmette-Guerin infections based on bacteria-specific labeling and sonotheranostic strategy. *Int J Nanomedicine*. 2021;16:6553–6573. doi:10.2147/IJN.S321631
31. Bowerman CJ, Byrne JD, Chu KS, et al. Docetaxel-loaded PLGA nanoparticles improve efficacy in taxane-resistant triple-negative breast cancer. *Nano Lett*. 2017;17(1):242–248. doi:10.1021/acs.nanolett.6b03971
32. Girvan AC, Teng Y, Casson LK, et al. AGRO100 inhibits activation of nuclear factor-kappaB (NF-kappaB) by forming a complex with NF-kappaB essential modulator (NEMO) and nucleolin. *Mol Cancer Ther*. 2006;5(7):1790–1799. doi:10.1158/1535-7163.MCT-05-0361
33. Geremia I, Pavlenko D, Maksymow K, Rüth M, Lemke HD, Stamatialis D. Ex vivo evaluation of the blood compatibility of mixed matrix haemodialysis membranes. *Acta Biomater*. 2020;111:118–128. doi:10.1016/j.actbio.2020.05.016
34. Thanh VM, Nguyen TH, Tran TV, et al. Low systemic toxicity nanocarriers fabricated from heparin-mPEG and PAMAM dendrimers for controlled drug release. *Mater Sci Eng C Mater Biol Appl*. 2018;82:291–298. doi:10.1016/j.msec.2017.07.051
35. Ugrinova I, Petrova M, Chalabi-Dchar M, Bouvet P. Multifaceted nucleolin protein and its molecular partners in oncogenesis. *Adv Protein Chem Struct Biol*. 2018;111:133–164.
36. Chen Z, Xu X. Roles of nucleolin: focus on cancer and anti-cancer therapy. *Saudi Med J*. 2016;37(12):1312–1318. doi:10.15537/smj.2016.12.15972
37. Varty K, O'Brien C, Ignaszak A. Breast cancer aptamers: current sensing targets, available aptamers, and their evaluation for clinical use in diagnostics. *Cancers*. 2021;13(16):3984. doi:10.3390/cancers13163984
38. Yang Y, Jing L, Li X, Lin L, Yue X, Dai Z. Hyaluronic acid conjugated magnetic Prussian Blue@Quantum Dot nanoparticles for cancer theranostics. *Theranostics*. 2017;7(2):466–481. doi:10.7150/thno.17411
39. Tang H, Guo Y, Peng L, et al. In vivo targeted, responsive, and synergistic cancer nanotheranostics by magnetic resonance imaging-guided synergistic high-intensity focused ultrasound ablation and chemotherapy. *ACS Appl Mater Interfaces*. 2018;10(18):15428–15441. doi:10.1021/acsami.8b01967
40. Cao Y, Chen Y, Yu T, et al. Drug release from phase-changeable nanodroplets triggered by low-intensity focused ultrasound. *Theranostics*. 2018;8 (5):1327–1339. doi:10.7150/thno.21492
41. Yildirim A, Shi D, Roy S, et al. Nanoparticle-mediated acoustic cavitation enables high intensity focused ultrasound ablation without tissue heating. *ACS Appl Mater Interfaces*. 2018;10(43):36786–36795. doi:10.1021/acsami.8b15368
42. Chen Y, Chen H, Shi J. Nanobiotechnology promotes noninvasive high-intensity focused ultrasound cancer surgery. *Adv Healthc Mater*. 2015;4 (1):158–165. doi:10.1002/adhm.201400127
43. Goodwin AP, Nakatsuka MA, Mattrey RF. Stimulus-responsive ultrasound contrast agents for clinical imaging: motivations, demonstrations, and future directions. *Wiley Interdiscip Rev Nanomed Nanobiotechnol*. 2015;7(1):111–123. doi:10.1002/wnan.1285
44. Dogan BE, Turnbull LW. Imaging of triple-negative breast cancer. *Ann Oncol*. 2012;23 Suppl 6:vi23–vi29. doi:10.1093/annonc/mds191
45. Rosenthal I, Sostaric JZ, Riesz P. Sonodynamic therapy – a review of the synergistic effects of drugs and ultrasound. *Ultrason Sonochem*. 2004;11 (6):349–363. doi:10.1016/j.ultsonch.2004.03.004
46. Matafonova G, Batoev V. Review on low- and high-frequency sonolytic, sonophotolytic and sonophotochemical processes for inactivating pathogenic microorganisms in aqueous media. *Water Res*. 2019;166:115085. doi:10.1016/j.watres.2019.115085
47. Srinivas US, Tan BWQ, Vellayappan BA, Jeyasekharan AD. ROS and the DNA damage response in cancer. *Redox Biol*. 2019;25:101084. doi:10.1016/j.redox.2018.101084
48. Sosa V, Moliné T, Somoza R, Paciucci R, Kondoh H, LLeonart ME. Oxidative stress and cancer: an overview. *Ageing Res Rev*. 2013;12 (1):376–390. doi:10.1016/j.arr.2012.10.004
49. Pastushenko I, Blanpain C. EMT transition states during tumor progression and metastasis. *Trends Cell Biol*. 2019;29(3):212–226. doi:10.1016/j.tcb.2018.12.001
50. Musaelyan A, Lapin S, Nazarov V, et al. Vimentin as antigenic target in autoimmunity: a comprehensive review. *Autoimmun Rev*. 2018;17 (9):926–934. doi:10.1016/j.autrev.2018.04.004

51. Satelli A, Li S. Vimentin in cancer and its potential as a molecular target for cancer therapy. *Cell Mol Life Sci*. 2011;68(18):3033–3046. doi:10.1007/s00018-011-0735-1
52. Gong C, Yang B, Shi Y, et al. Factors influencing the ablative efficiency of high intensity focused ultrasound (HIFU) treatment for adenomyosis: a retrospective study. *Int J Hyperthermia*. 2016;32(5):496–503. doi:10.3109/02656736.2016.1149232
53. Chitnis PV, Farny CH, Roy RA. SVD-based separation of stable and inertial cavitation signals applied to passive cavitation mapping during HIFU. *IEEE Trans Ultrason Ferroelectr Freq Control*. 2019;66(5):857–866. doi:10.1109/TUFFC.2019.2898917
54. Xu S, Chang N, Wang R, et al. Acoustic droplet vaporization and inertial cavitation thresholds and efficiencies of nanodroplets emulsions inside the focused region using a dual-frequency ring focused ultrasound. *Ultrason Sonochem*. 2018;48:532–537. doi:10.1016/j.ultsonch.2018.07.020
55. Holt RG, Roy RA. Measurements of bubble-enhanced heating from focused, MHz-frequency ultrasound in a tissue-mimicking material. *Ultrasound Med Biol*. 2001;27(10):1399–1412. doi:10.1016/S0301-5629(01)00438-0
56. Farny CH, Glynn Holt R, Roy RA. The correlation between bubble-enhanced HIFU heating and cavitation power. *IEEE Trans Biomed Eng*. 2010;57(1):175–184. doi:10.1109/TBME.2009.2028133
57. Coussios CC, Farny CH, Haar GT, Roy RA. Role of acoustic cavitation in the delivery and monitoring of cancer treatment by high-intensity focused ultrasound (HIFU) [published correction appears in Int J Hyperthermia. 2007 May;23(3):327]. *Int J Hyperthermia*. 2007;23(2):105–120. doi:10.1080/02656730701194131
58. Tang J, Guha C, Tomé WA. Biological effects induced by non-thermal ultrasound and implications for cancer therapy: a review of the current literature. *Technol Cancer Res Treat*. 2015;14(2):221–235. doi:10.7785/tcrt.2012.500407
59. Dittmar KM, Xie J, Hunter F, et al. Pulsed high-intensity focused ultrasound enhances systemic administration of naked DNA in squamous cell carcinoma model: initial experience. *Radiology*. 2005;235(2):541–546. doi:10.1148/radiol.2352040254
60. Riesz P, Kondo T. Free radical formation induced by ultrasound and its biological implications. *Free Radic Biol Med*. 1992;13(3):247–270. doi:10.1016/0891-5849(92)90021-8
61. Honda H, Kondo T, Zhao QL, Feril LB Jr, Kitagawa H. Role of intracellular calcium ions and reactive oxygen species in apoptosis induced by ultrasound. *Ultrasound Med Biol*. 2004;30(5):683–692. doi:10.1016/j.ultrasmedbio.2004.02.008
62. Wang P, Wang X, Liu Q, Zhao X, Cao B, Zhao P. Comparison between sonodynamic effects with protoporphyrin IX and hematoporphyrin on the cytoskeleton of Ehrlich ascites carcinoma cells. *Cancer Biother Radiopharm*. 2010;25(1):55–64. doi:10.1089/cbr.2008.0604
63. Hu Z, Yang XY, Liu Y, et al. Investigation of HIFU-induced anti-tumor immunity in a mice tumor model. *J Transl Med*. 2007;5(1):34. doi:10.1186/1479-5876-5-34
64. Lu P, Zhu XQ, Xu ZL, Zhou Q, Zhang J, Wu F. Increased infiltration of activated tumor-infiltrating lymphocytes after high intensity focused ultrasound ablation of human breast cancer. *Surgery*. 2009;145(3):286–293. doi:10.1016/j.surg.2008.10.010
65. van den Bijgaart RJ, Eikelenboom DC, Hoogenboom M, Fütterer JJ, den Brok MH, Adema GJ. Thermal and mechanical high-intensity focused ultrasound: perspectives on tumor ablation, immune effects and combination strategies. *Cancer Immunol Immunother*. 2017;66(2):247–258. doi:10.1007/s00262-016-1891-9
66. Ji R, Karakatsani ME, Burgess M, Smith M, Murillo MF, Konofagou EE. Cavitation-modulated inflammatory response following focused ultrasound blood-brain barrier opening. *J Control Release*. 2021;337:458–471. doi:10.1016/j.jconrel.2021.07.042
67. Chen KT, Wei KC, Liu HL. Focused ultrasound combined with microbubbles in central nervous system applications. *Pharmaceutics*. 2021;13(7):1084. doi:10.3390/pharmaceutics13071084
68. Tang H, Zheng Y, Chen Y. Materials chemistry of nanoultrasonic biomedicine. *Adv Mater*. 2017;29(10):1604105. doi:10.1002/adma.201604105
69. Chen Y, Ye D, Wu M, et al. Break-up of two-dimensional MnO2 nanosheets promotes ultrasensitive pH-triggered theranostics of cancer. *Adv Mater*. 2014;26(41):7019–7026. doi:10.1002/adma.201402572
70. Li J, Arnal B, Wei CW, et al. Magneto-optical nanoparticles for cyclic magnetomotive photoacoustic imaging. *ACS Nano*. 2015;9(2):1964–1976. doi:10.1021/nn5069258
71. Nomikou N, McHale AP. Exploiting ultrasound-mediated effects in delivering targeted, site-specific cancer therapy. *Cancer Lett*. 2010;296(2):133–143. doi:10.1016/j.canlet.2010.06.002
72. Sheybani ND, Price RJ. Perspectives on recent progress in focused ultrasound immunotherapy. *Theranostics*. 2019;9(25):7749–7758. doi:10.7150/thno.37131